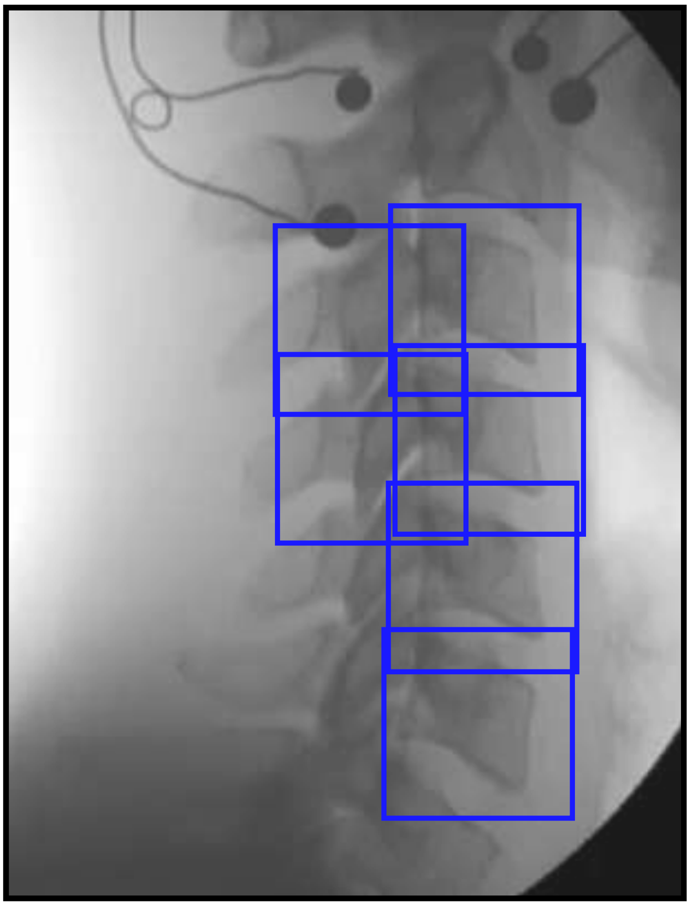

AALBORG UNIVERSITY
STUDENT REPORT

18gr9441 Master's Thesis
Ida Marie Groth Jakobsen

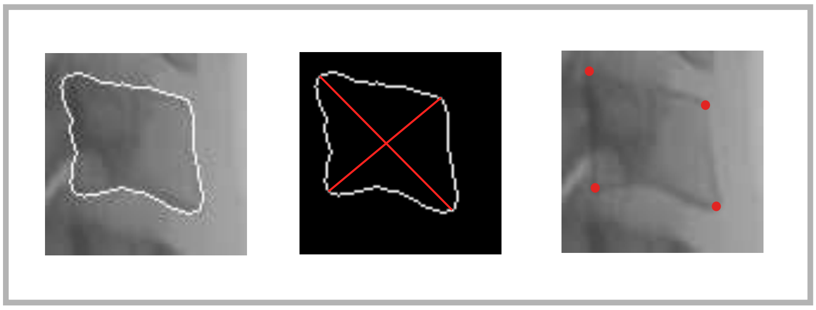

Automatic corner detection of the cervical vertebrae C2-C7 in fluoroscopic recordings

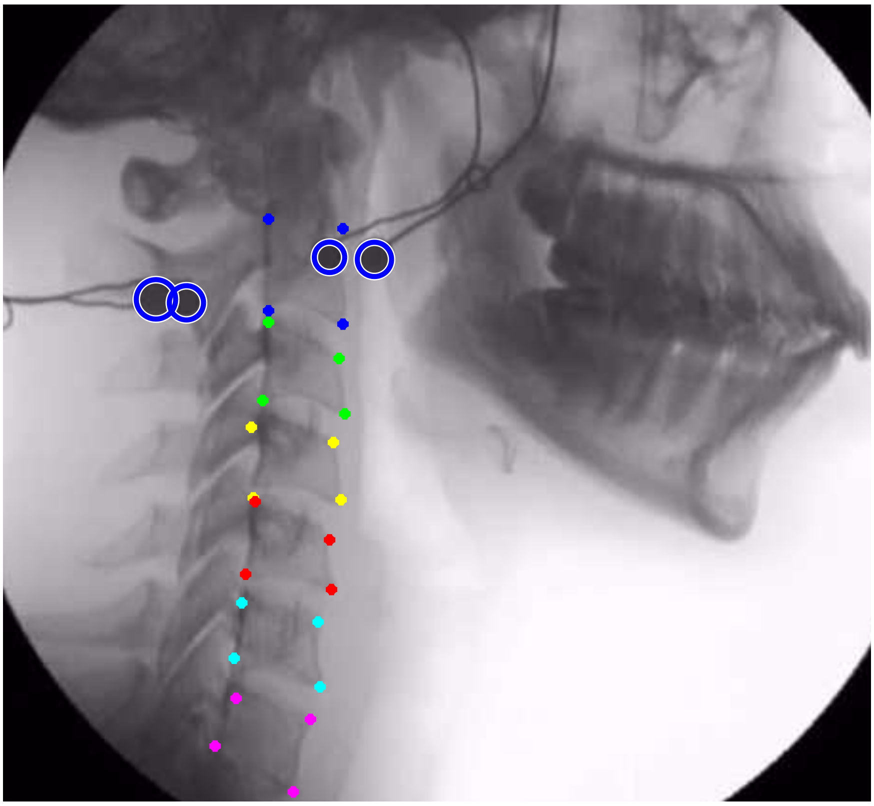

Aalborg University
4th semester M.Sc.
Biomedical Engineering & Informatics

January 2019

AALBORG UNIVERSITY
STUDENT REPORT

School of Medicine and Health
Biomedical Engineering and Informatics
Niels Jernes Vej 12, 5A
9220 Aalborg Ø
Phone: 9940 8752
http://smh.aau.dk

Title: Automatic corner detection of the cervical vertebrae C2-C7 in fluoroscopic recordings

Theme: Master's thesis

Project period: 4^{th} semester M.Sc., Autumn 2018

Project group: 18gr9441

Participant:

Ida Marie Groth Jakobsen

Supervisor:
Maciej Plocharski

Number of pages: 45

Submission date: 3^{rd} of January 2019

Abstract:

Neck pain has great economical consequences but due to the relationship between intervertebral motion and the functionality of the spine, investigating the rotation and translation of adjacent vertebrae can be used to determine the underlying cause. Fluoroscopic imaging can, with the high number of images taken, provide a more accurate reflection of the intervertebral motion than other imaging modalities. The estimation of the rotation and translation most often depends on the localization of four landmarks, which are usually the corner points of the vertebral bodies in the cervical spine. The detection of the landmarks is usually based on manual markings, which can be a tedious process.
The aim of the present study was to detect the landmarks of the cervical vertebrae C2-C7 in fluoroscopic recordings. Four subjects performed extension and flexion of the neck while wearing glasses with external markers for the occiput. The center points of the external markers and the four landmarks of C3-C6 along with the inferior corner points of C2 and superior corner points of C7 were automatically detected. The landmarks were detected using a multi-segmentation approach and the automatic detection method was tested on five frames of each fluoroscopic recording. The external markers were detected correctly in 27 of the 40 tested frames while the corners of the cervical vertebrae were detected in 31 frames. The method shows, that it is possible to detect the cervical vertebrae without manual interaction.

Resumé

Nakke- og lændesmerter er nogle af de største sundhedsproblemer i verden, hvad angår økonomiske udgifter. Langtidssygemeldinger og udgifter til behandling er nogle af dem, men også socialt, fysisk og mentalt kan smerterne have en indvirkning på livskvaliteten hos den ramte. Behandlingen af nakkesmerter kræver bestemmelse af den underliggende årsag. Dette gøres gennem patientens egen redegørelse for forløbet samt en fysisk undersøgelse af nakken. Klarlægges årsagen ikke herigennem, benyttes ofte en billeddiagnostisk undersøgelse.

Ved undersøgelse af nakkehvirvlernes rotation og forskydning i forhold til hinanden, kan opnåes viden om rygsøjlens normale og unormale bevægemønstre, som kan hjælpe med at bestemme årsagen til smerterne. Ved hjælp af fluoroskopi, kan rotationen og forskydningen undersøges, mens personen bevæger hovedet fremover eller bageover. Bevæglesen under billedtagningen, giver et mere sandfærdigt billede af nakkehvirvlernes dynamikker end statiske billedteknikker, men resulterer også i en dårligere billedkvalitet. Oftest benyttes almindelige røntgenbilleder til at undersøge nakkehvirvlene, da billedkvaliteten er bedre, men er begrænset af at personen skal sidde stille under billedtagningen. Fluoroskopi benyttes oftere til at undersøge de større lændehvirvler.

Bestemmelsen af nakkehvirvlernes rotation og forskydning, er typisk baseret på markeringer af hjørnepunkterne på hvert hvirvellegeme. Markeringerne er ofte manuelt bestemt, hvilket kan være en langsommelig og anstrængende proces. Nakkehvirvlernes anatomi adskiller sig fra rygsøjlens andre hvirvler, idet C1, tættest på kraniet, ikke har et hvirvellegeme, samt den øverste del af C2, ofte er svær at adskille fra C1 på et fluoroskopibillede. Derudover kan den nederste del af den syvende nakkehvirvel, C7, være skjult bag skulderen. Nakkens hvirvellegemer er desuden de mindste, og er karakteriseret ved en tværgående åbning på siderne, som gør det svært at adskille særligt den bageste kant fra resten. Der er ikke fundet nogen studier der beskriver, hvordan nakkehvirvlernes hjørnepunkter automatisk kan lokaliseres og markeres i fluoroskopibilleder.

Formålet med dette studie var, automatisk at finde og markere hjørnepunkterne på nakkehvirvlerne C2-C7 i fluoroskopibilleder. Fire forsøgspersoner udførte hver en bevægelse fremover med hovedet og en bagover under optagelsen af en række fluoroskopibilleder. Forsøgspersonerner bar briller med fire metalkugler, der udgjorde eksterne markører for baghovedet. Centrum af hver ekstern markør, fire hjørnepunkter af nakkehvirvlerne C3-C6 samt de to nederste hjørnepunkter for C2 og de to øverste for C7 blev automatisk fundet og markeret i fluoroskopibillederne. Hjørnepunkterne blev fundet ved hjælp af en metode, hvor den bedste af flere segmenteringer, blev benyttet til at bestemme kanten af hvert hvirvellegeme. Fem billeder fra hver fluoroskopisk optagelse, blev brugt til at teste den automatiske metode. De eksterne markører blev fundet korrekt i 27 af de 40 testede billeder og hjørnepunkterne blev fundet i 31 af billederne. Resultaterne viser at det er muligt at finde og markere nakkehvirvlerne uden manuel påvirkning i fluoroskopiske billeder.

Preface

This master's thesis is completed by a student on the 4^{th} semester M.Sc. in Biomedical Engineering and Informatics, Aalborg University, in the time period 1^{st} of September 2018 till 3^{rd} of January 2019.

A special thanks to Jonas Groth Jakobsen, M.Sc. in Computer Science for technical support.

Reading guide

In this master's thesis, references are cited using the Harvard Method. A reference placed within a sentence is only a reference for the content of the sentence in question. If the reference is placed after the period of a sentence, it is applicable to the whole section, beginning from the last stated reference in the chapter.

The project is organized into six chapters. Chapters 1 and 2 cover the background of the problem area, chapter 3 defines the problem to be solved, and chapters 4 and 5 present a proposed solution of the problem and the results. Chapter 6 discusses the solution leading to a final conclusion.

All drawn figures are constructed by the author. If the figure is based on a reference, this will be emphasized.

List of content

Chapter 1

Introduction

Back pain is a worldwide health problem with great economical consequences due to sick leave for extensive time spans, GP consultations, treatment expenses, premature retirements and expenses due to loss of productivity. [Flachs et al., 2015, Hurwitz et al., 2018, Hoy et al., 2014a,b] A review by Hurwitz et al. found that low back and neck pain are generally the leading cause of productive years lost due to disability. [Hurwitz et al., 2018] That is consistent with studies by Hoy et al. [2014a, 2014b] who found that out of 291 conditions, low back pain is the highest ranked disorder in terms of productive years lost due to disability with a point prevalence of 9.4 %, whereas neck pain is ranked fourth with a point prevalence of 4.9 %. In terms of disability-adjusted life years, they ranked sixth and 21st, respectively. [Hoy et al., 2014a,b]

In Denmark, 10 % of all visits to the GP are due to low back pain and 6 % are due to neck pain. They account for 20 % and 16 % of all sick leaves, respectively and one in five has over a time period of two years been on long-term sick leave. Back pain causes annually more than 1,100 early retirements, constituting almost 8 % of the total number. Expenses to treatment amount to more than 430 mio. dollars and expenses due to lost productivity exceed one billion dollars. [Flachs et al., 2015] In addition to the economic burden of back pain, it can have a huge impact on the social life, physical abilities and psychological well-being of the individual. [Genebra et al., 2017]

The initial clinical investigation of neck pain includes anamnestic information, duration of the condition, physical examination and exclusion of severe pathology. The latter is only the cause in less than one percent of the cases. Radiography (X-ray) of the cervical region is the most widely used imaging modality when the examination requires visualization, but other imaging modalities, such as Computed Tomography (CT), Magnetic Resonance Imaging (MRI) or Single Photon Emission Computer Tomography (SPECT) are also utilized. [Kjær et al., 2010]

The prevalence of neck pain is expected to increase and greater knowledge regarding predictors and causes is required, as well as how to improve the management of neck pain or even prevent it. [Hoy et al., 2014b, Hurwitz et al., 2018]

The dynamic behavior of the spinal segments provides information about the functionality of the spine, thus, by studying the intervertebral motion, knowledge regarding normal as well as abnormal mechanics of the spine can be gained. [Cerciello et al., 2009, Bifulco et al., 2001] The motion or kinematics depends on the muscles, discs, ligaments and vertebrae of the spine and is described by rotation and translation evaluated between adjacent vertebrae. [Bifulco et al., 2001, Frobin et al., 1996] The relationship between back pain and intervertebral motion has been acknowledged for decades and by examining the kinematics, the underlying cause of back pain can be investigated. It is essential to evaluate the correlation between clinical symptoms and intervertebral kinematics to obtain a greater understanding and thereby improvement of the mechanisms of treatment of neck pain. However, due to the spinal inaccessibility, indirect measurements, such as calculating rotational and translational movement of adjacent vertebrae by means of imaging, are required. [Breen et al., 2012, Bifulco et al., 2001, Anderst et al., 2013a, 2018]

Imaging is an essential tool for diagnosing spinal fractures, vertebral alignment, compression injuries and follow-up examinations. [Lisle, 2012] Especially imaging modalities that allow measurement during motion have shown to be of importance when studying back pain, due to more accurate calculations of rotation and translation. The intervertebral motion is closely related to the movement performed, causing the angle between adjacent vertebrae in a flexion movement to be significantly different from the angle in an extension movement in identical head orientations. This cannot be accurately represented by static imaging techniques. [Anderst et al., 2013a] When dynamic imaging is used for kinematic analysis, the detection and tracking are often based on manually selected vertebral landmarks, which can contribute to inaccuracy and thus, to errors in the calculations [Bifulco et al., 2001]. The landmarks, most frequently, the four corners of the vertebral bodies, are located in each frame, and although it can be a laborious and tedious process, a resent study, however, suggests high accuracy of the manual markings [Plocharski et al., 2018]. Furthermore, the manual markings are considered ground truth in several studies. [Cerciello et al., 2011, Lecron et al., 2012b, Kumar and Thomas, 2005]

In order to eliminate the laborious process of manually selected landmarks for the kinematic analysis, optimized methods to automatically detect the landmarks in medical images of the vertebrae are essential. The aim of this study is to develop a method which automatically detects the corners of the vertebral bodies in the cervical spine.

Chapter 2

Problem analysis

This chapter is comprised of an introduction to the basic anatomy of the spine with main emphasis on the cervical vertebrae. Subsequently, a brief description of imaging modalities used for evaluation of intervertebral kinematics will be presented. Finally, a definition of the landmarks along with different methods for vertebral detection with varying degree of manual interaction will be explicated.

2.1 The vertebral anatomy

The vertebral column is a part of the axial skeleton. It consists of 24 vertebrae, the sacrum and the coccyx. The spinal column provides support and stability, and it protects the spinal cord. The vertebrae are divided into five regions, as illustrated in *Figure 2.1*. The cervical region is composed of seven vertebrae C1 to C7. 12 vertebrae constitute the thoracic region (T1 to T12), five lumbar vertebrae (L1 to L5), the sacral and the coccygeal region. The sacral and coccygeal regions constitute a curve (sacral curve) along with each of the other three regions. The thoracic and sacral curves are primary, as they are present at birth, and curve posteriorly, whereas the cervical and lumbar curves are secondary, appearing several months after birth and curve anteriorly to compensate for the weight in an upright position. All four curves are not fully developed until the age of 10. [Martini et al., 2012]

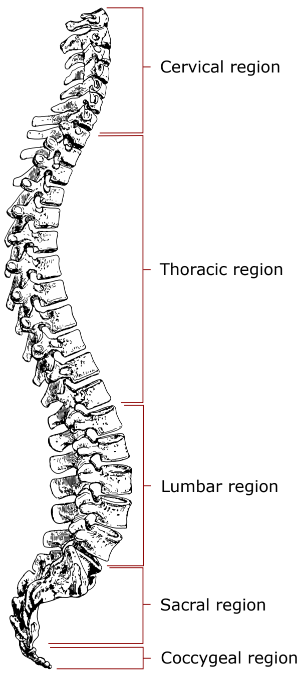

Figure 2.1: The five regions of the vertebral column; the cervical, thoracic, lumbar, sacral and the coccygeal region. Modified from Colourbox.

The cervical, thoracic and lumbar regions are comprised of individual vertebrae, each consisting of a **vertebral body**, **articular processes** as well as a **vertebral arc** formed by the pedicles and laminae (an example of a cervical vertebra is illustrated in *Figure 2.2*). The vertebral body is the weight-bearing and -transferring part of the vertebra. The bodies of adjacent vertebrae are separated by intervertebral discs, consisting of fibrocartilage. Since the lumbar region supports the heaviest load, the vertebral bodies in the caudal part of the vertebral column are the largest, decreasing in the cranial direction. Together with the body, the vertebral arch constitutes the vertebral foramen, which is greatest in the cervical region and decreasing downwards due to the diameter of the spinal cord. The articular processes of adjacent inferior and superior vertebrae constitutes the intervertebral articulations. [Martini et al., 2012]

2.1.1 The cervical vertebrae

The cervical vertebra C1, closest to the skull, is also called atlas and differs from other vertebrae due to the lack of a body and spinous processes. Instead, an anterior and posterior arch constitute the large vertebral foramen. The articulation between the skull and the atlas permits flexion and extension movements or nodding, whereas the articulation between the atlas and the axis (C2) permits a rotational movement or shaking of the head because of the dens on the body of the axis. The cervical vertebrae C3 to C6 are more similar with small oval-shaped vertebral bodies shown in *Figure 2.2* as well as transverse foramina that gives passage to blood vessels and nerves. The C7 has large transverse processes for muscle attachment and the spinous process is long and slender with greater resemblance to the spinous processes of the thoracic vertebrae. [Martini et al., 2012, Reinartz et al., 2009]

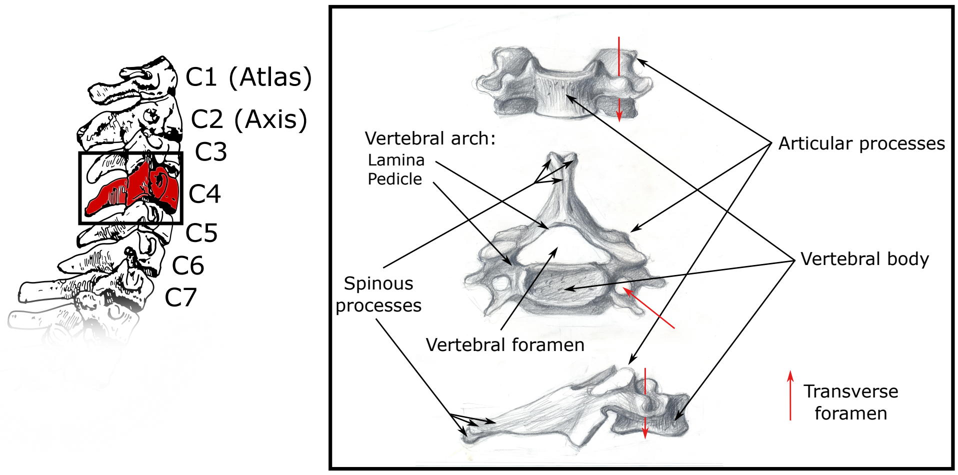

Figure 2.2: To the left; an overview of the cervical vertebrae C1 to C7. To the right; the anatomy of the fourth cervical vertebra (C4) is presented in anterior view (top), superior view (middle) and lateral view (bottom). Modified from Colourbox.

2.2 Intervertebral kinematics of the neck

Individual intervertebral articulations have a relatively small range of motion (ROM) but their combined mobility provides great flexibility and is very strong. The vertebrae in the cervical region permit greater flexibility than any of the other regions. Controlled head movement is due to a great number of ligaments and small muscles in the neck, but rapid change in head position, caused by extreme acceleration or deceleration, can result in injuries to the vertebrae, fractures or dislocations, commonly referred to as whiplash.
The intervertebral articulations in the cervical region permit several types of movement. **Flexion** is movement in the anterior-posterior plane and decreases the angle between the

intervertebral articulations. **Extension** is movement in the same plane but in the opposite direction, which increases the angle until anatomical position. A further extension of the intervertebral articulations of the neck is called **hyperextension**. The intervertebral articulations also allow for left and right axial **rotation** of the head and, finally, **lateral flexion**. These types of movement are illustrated in *Figure 2.3*.

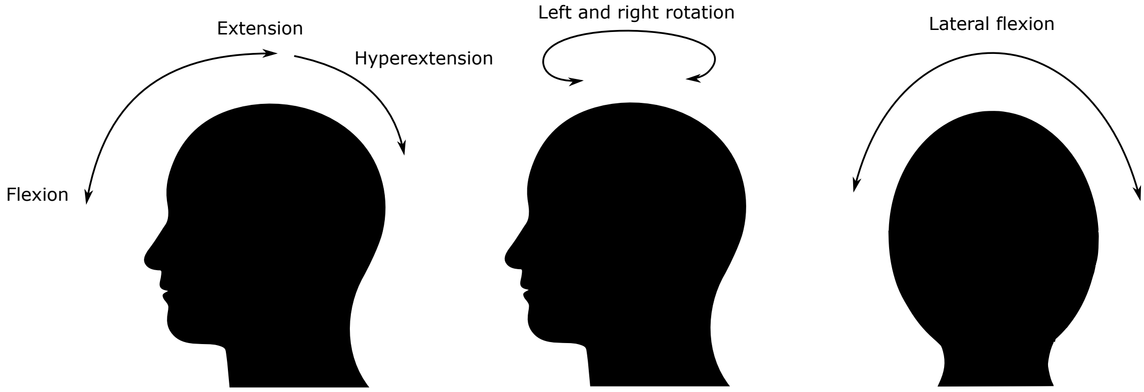

Figure 2.3: To the left; an illustration of the flexion and extension movement of the cervical region. In the middle is shown the axial rotation and to the right; the lateral flexion of the cervical region.

Apart from the angular movement between the intervertebral articulations during flexion-extension movements, the intervertebral discs between the bodies of adjacent vertebrae permit minor gliding movements or translation. [Martini et al., 2012] Together, the rotational and translational movements have six degrees of freedom; three rotations: twist, flexion-extension and lateral flexion as shown in Figure 2.3; and three translations: anterior-posterior, medial-lateral and superior-inferior. [Anderst et al., 2013b]
Factors that have been proven to affect spinal flexibility include gender, height, obesity and intervertebral disc height, which is related to age. [Battié et al., 1987, Martini et al., 2012]

The functionality of the spine provides important information in the process of diagnosing the cause of back and neck pain as well as evaluating treatment methods. The functionality can be investigated by measuring the intervertebral kinematics of adjacent vertebrae by means of flexion and extension movements of the spine in sagittal plane, as these movements are assumed to be planar motions. [Cerciello et al., 2009, Bifulco et al., 2001, Breen et al., 2012, Lisle, 2012]

2.3 Imaging techniques

The type of imaging technique selected for examination of neck pain is dependent on the suspected type of injury. MRI is utilized when the pain is caused by soft tissue injuries such as nerve root damage or spinal abnormalities due to the great soft tissue contrast. Furthermore, MRI has the advantage that the patient is not exposed to ionizing radiation, as opposed to CT and radiography. CT is the imaging technique of choice when a high level of detail is required, such as in assessment of minor bone fractures or spinal tumors. [Lisle, 2012]

Radiographic imaging is the most widely used modality for examining the cause of neck pain. Radiography is also known as X-rays and is an inexpensive and fast imaging modality, well-suited for viewing the majority of bone structures. Higher image quality can be obtained by regulating different factors, including an increase in the radiation dose, which can be harmful to the patient, and therefore image quality and patient safety must be well-balanced [Bushberg et al., 2011, Chen et al., 2010]. The radiation exposure to the patient also limits the number of acquired radiographic images. [Lisle, 2012, Chen et al., 2010, Chowdhury et al., 2010]

2.3.1 Fluoroscopy

Fluoroscopic imaging is based on radiography, where a sequence of digital X-ray images, with up to 30 frames per second (continuous fluoroscopy), can provide a video that, by the human eye, is perceived as continuous. For lower radiation dose exposure, especially desired in pediatrics, pulsed fluoroscopy with typically 15 frames per second, is often used [Aichinger et al., 2012]. Fluoroscopy is useful during procedures where high precision is required, such as positioning a catheter for angiography and visualizing the contrast agent as it is injected into the vessel through the catheter. [Bushberg et al., 2011, Lisle, 2012, Chen et al., 2010, Chowdhury et al., 2010]

The high number of images, captured during a fluoroscopic recording, requires a low radiation dose, which is considerably smaller than the one in radiography. Due to the reduced radiation, the image quality is simultaneously reduced. To compensate, a sensitive low-noise image receptor system is required, often an image intensifier. [Bushberg et al., 2011, Lisle, 2012, Chen et al., 2010, Chowdhury et al., 2010] Furthermore, the motion performed during continuous fluoroscopy causes blur and can impede subsequent image processing. [Aichinger et al., 2012, Xue and Wilson, 1998] In the conventional continuous fluoroscopy, the motion blur is more distinct, whereas in pulsed fluoroscopy it is greatly reduced, as the movement is frozen in each frame. [Jones, 2014, Xue and Wilson, 1998]

For assessment of suspected injury of the neck, lateral cervical spine radiographs are the most commonly used, but when studying the rotation and translation of adjacent vertebrae, images of neutral position and at the end range of flexion and extension, using static imaging modalities, are insufficient. This is due to the difference in the angle of adjacent vertebrae during flexion compared to an extension movement with similar head orientation, thus fluoroscopy is ideal for the assessment of intervertebral kinematics. [Anderst et al., 2013a] Determining the cause of back pain can be difficult, but by assessing vertebral kinematics, by means of fluoroscopy, information about normal as well as altered spinal motion can assist in finding the underlying cause. [Cerciello et al., 2011, Bifulco et al., 2001]

2.4 Assessment of vertebral kinematics

The method to assess vertebral kinematics, by determining the translation and rotation of adjacent vertebrae in the sagittal plane, is based on location of four landmarks: two ventral and two dorsal corner points of the vertebral body in a lateral view, as illustrated in *Figure 2.4*. A ventral and a dorsal midpoint along with a center point is located for each vertebra. For the calculations of rotation and translation, the midplanes and the bisectrix of adjacent vertebrae are found. The method is independent to distortion, axial rotation and lateral tilt. [Frobin et al., 1996]

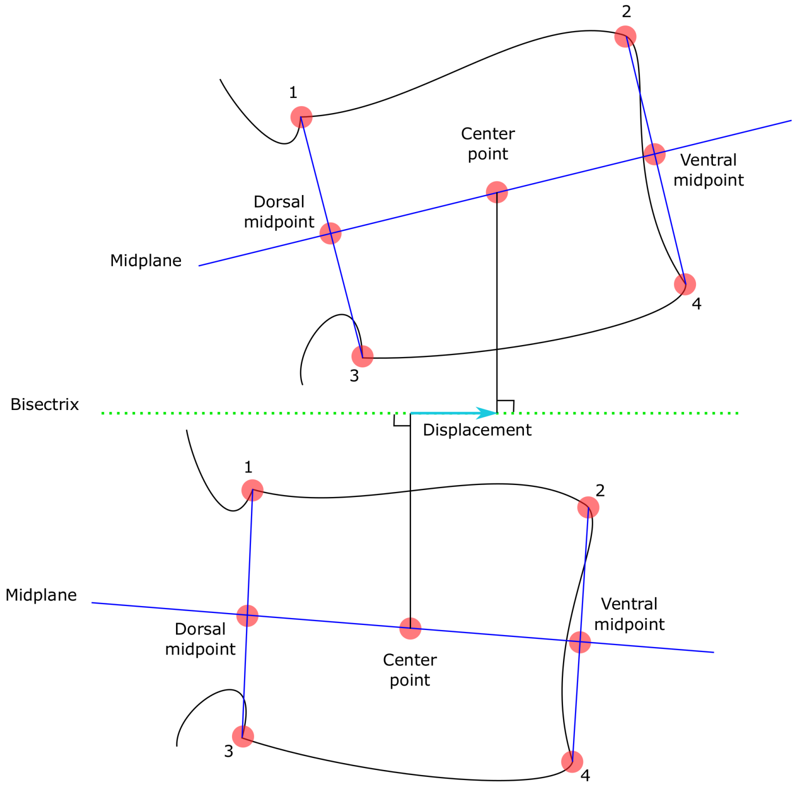

Figure 2.4: The landmark-based method described by Frobin et al., where the four corners of the vertebral body are localized in a lateral view. The midpoint between the two dorsal and the two ventral points are found. A line through these two midpoints and a center point constitute the midplane. The angle between the midplanes of two adjacent vertebrae is used for the calculation of the rotation. The two center points are projected perpendicular onto the bisectrix of two midplanes, and the distance between the projections is the displacement used for the calculation of translation. Adapted from [Frobin et al., 1996]

To calculate the rotational and translational movement of adjacent vertebrae, the localization of the four landmarks on each vertebra is necessary, whereas the center point and the midplane can be derived from the landmarks. The angular rotation is calculated on the basis of the angle between the midplanes of two adjacent vertebrae and is the difference between these angles in extension and flexion. The angle is positive in extension and negative in flexion. Translation is the dorsoventral displacement and is calculated on the basis of the perpendicular projections of the center points onto the bisectrix of two adjacent midplanes, and the displacement is the distance between these two projections. To take differences in magnifications into account, the displacement is converted to a dimensionless measure by dividing with the mean depth of the most cranial vertebra. [Frobin et al., 2002]

The anatomical shape of C1 and C2 differs from the remaining vertebra, as C1 lacks a vertebral body and C1 and C2 often appear as a single vertebra in the images. The markings of C1 is, thus, two landmarks, one marking the anterior arch and one marking the posterior arch. When the superior corners of C2 are indistinguishable from C1, only the inferior corners are used as landmarks. Furthermore, the inferior part of C7 is often obscured by the shoulder, and in that case only the superior corners constitute the landmarks. [Plocharski et al., 2018, Nøhr et al., 2017] *Figure 2.5* presents an example of a frame from a fluoroscopic recording where the superior corners of the vertebral body C2 are difficult to separate from C1, and the inferior corners of C7 are obscured by the shoulder.

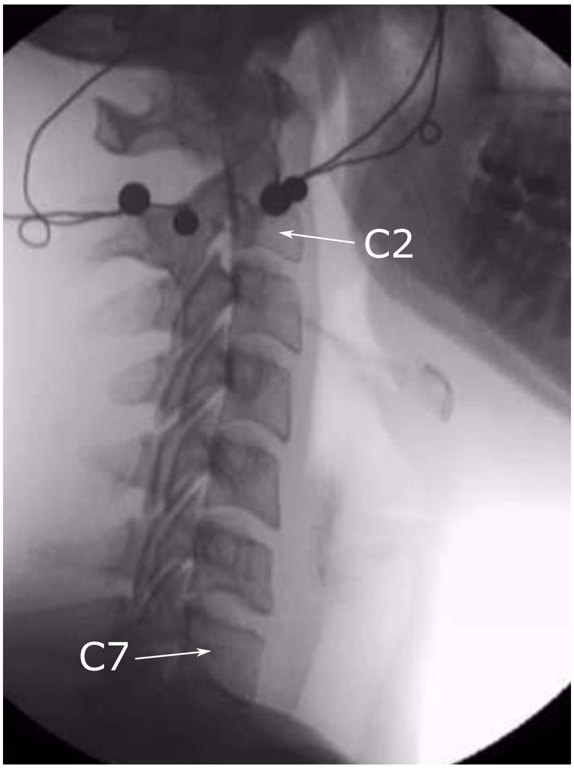

Figure 2.5: The superior vertebral corners of C2 are indistinguishable from C1 and the inferior corners of C7 are obscured by the shoulder of the subject, thus only two of the vertebral corners constitute the landmarks for each vertebra.

Several methods for vertebral detection, with varying degree of manual interaction, have been described, but in the following only a selection of those using radiographic or fluoroscopic images are described.

2.4.1 Manual detection methods

The detection of the vertebral landmarks is often a manual process, which can be laborious and tedious [Bifulco et al., 2001]. However, the advantage of the manual markings is that they can be highly reliable, and they are often considered as ground truth. [Cerciello et al., 2011, Lecron et al., 2012b, Kumar and Thomas, 2005] Even when the markings are performed by someone without previous anatomical knowledge, the manual detection of the vertebral corners can be very accurate. [Wang et al., 2018, Plocharski et al., 2018]

Two studies used fluoroscopic videos for the investigation of intervertebral kinematics in the cervical region [Wang et al., 2018, Plocharski et al., 2018]. In a frame, 22 points were manually marked and used for the calculations along with four external markings. The intra-rater reliability was determined by three repeated markings of the landmarks for the neutral position, mid-range of both flexion and extension movement and for the end-range of both flexion and extension. The intra-class correlation was above 0.97 in all five positions. [Wang et al., 2018] Both the intra- and the inter-rater marking errors were low and the results suggest that high precision markings of the vertebral landmarks can be obtained without former experience in radiographic image analysis. [Plocharski et al., 2018]

However, manual localization of the landmarks in each frame in a series of fluoroscopic images is a tedious process, and in large data sets the manual approach is often prone to errors, causing the results to be inaccurate. [Bifulco et al., 2001]

2.4.2 Semi-automatic detection methods

Various semi-automatic methods for vertebral detection and tracking are emerging, and fluoroscopic images are widely used for studying the intervertebral kinematics in the lumbar region. Different manual interactions are performed, but often the detection of the vertebrae is fully manualized by marking the four landmarks of each vertebral body and then by automatically tracking the vertebrae in the following frames. The manual markings are frequently used to generate a template for the tracking or as initial contour for active contour segmentation. [Bifulco et al., 2001, 2009, 2012, Cerciello et al., 2009, 2011, Breen et al., 2012]

Detection and tracking of the smaller cervical vertebrae are often conducted by using X-ray images due to the higher image quality. Regions of interest in the image are often constructed by manual markings of either the center or the corners of each vertebral body. [Al-Arif et al., 2015a,b, Benjelloun and Mahmoudi, 2008] A higher degree of manual interaction is utilized when a manually constructed template is matched to a manual definition of the regions of interest in the image. [Larhmam et al., 2012, 2013]. Due to the difficulties associated with the tracking of the cervical vertebrae, it is often focused on C3-C7 [Al-Arif et al., 2015a,b, Benjelloun and Mahmoudi, 2008, Larhmam et al., 2012, 2013]

In fluoroscopy, the cervical vertebrae are often detected manually and tracked using a template [Bifulco et al., 2013, Reinartz et al., 2009, Nøhr et al., 2017] or corner detection [Nauman et al., 2017]. The template is selected manually, either by a user-drawn template of each vertebrae on a single frame [Bifulco et al., 2013, Reinartz et al., 2009], or by manually defined landmarks of the vertebral bodies in the first frame [Nøhr et al., 2017, Nauman et al., 2017]. Due to the lower quality of the fluoroscopic images, the result can be a focus on the tracking of the cervical vertebrae C3-C6 [Nauman et al., 2017].

2.4.3 Automatic detection methods

Automatic detection and tracking of the vertebrae, with no initial markings or other manual interaction, are difficult tasks. The anatomy of the lumbar vertebral bodies makes it easier to detect the four corners in noisy fluoroscopic images, due to the large size and no visual obstruction. In the cervical region, the transverse processes with the transverse foramen can impede the localization of the posterior corners of the smaller vertebral bodies in lateral view. Most often radiography is used for the detection and tracking of the vertebral bodies in the cervical area due to the higher image quality.

Zheng et al. detect and track the lumbar vertebrae automatically in fluoroscopic images. [Zheng et al., 2001] The remaining studies utilize X-ray images for the automatic detection of the vertebral bodies in the cervical region. The majority use machine learning in order to train a classifier on a large set of images. [Al-Arif et al., 2018, Xu et al., 2012, Lecron et al., 2012a,b] Finally, a detection of the cervical spine, also in X-ray images, only estimates the location and orientation of the spine and not the individual vertebrae. [Kumar and Thomas, 2005] The automatic methods for vertebral detection are summarized in *Table 2.1*.

Table 2.1: Automatic methods for vertebral detection

Author	Image modality	Region	Method	Results	Note
Zheng et al. [2001]	Fluoroscopy	Lumbar	Genetic algorithm and Hough transform	Edges of vertebral bodies	Validation missing
Al-Arif et al. [2018]	Radiography	Cervical	Machine learning, convolutional network	Segmentation of the vertebral bodies	8928 images were used for training
Xu et al. [2012]	Radiography	Cervical	Machine learning, Haar-like features and active appearance model	Segmentation of the vertebral bodies and spinous processes	9357 images were used for training
Lecron et al. [2012a] and Lecron et al. [2012b]	Radiography	Cervical	Edge polygonal approximation, Scale-invariant Feature Transform and Speeded-up Robust Features for a multi-class Support Vector Machine	Segmentation of the vertebral bodies	49 images were used for training
Kumar and Thomas [2005]	Radiography	Cervical	Top-hat and Radon transformations	Orientation and position of spine	The individual vertebral bodies are not found

In three of the automatic methods, different machine learning methods were used for the recognition of vertebral bodies. Machine learning requires excessive training data in order to obtain a robust classifier and, thus, an accurate vertebral detection. [Al-Arif et al., 2018] Only one of the described automatic methods used fluoroscopic images where they developed a method for detection of the lumbar vertebrae [Zheng et al., 2001]. The remaining methods all detected the cervical vertebrae in radiographic images, which, due to the higher radiation dose during image acquisition, compared to fluoroscopy, results in higher image quality.

Due to the important information of the rotational and translational movement of adjacent vertebrae during flexion and extension of the neck, fluoroscopic imaging is the most ideal modality. To eliminate the protracted and tedious process of manual markings of the landmarks, automatic detection methods are required. No studies investigating fully automatic detection the cervical vertebrae in fluoroscopic images have been found.

2.5 Summary of the problem area

Measurements of the intervertebral kinematics, such as rotation and translation of adjacent vertebrae, can provide information about the functionality of the cervical spine. To evaluate the rotation and translation during flexion and extension movements, two ventral and two dorsal corner points of the vertebral body constitute four landmarks, essential to the calculations.

Various methods have been proposed for manual, semi-automatic and automatic detection of the vertebral landmarks in the lumbar and cervical region using radiographic and fluoroscopic images. Out of the presented fully automatic methods, only one study uses fluoroscopic images to analyze the vertebrae of the lumbar region, which, due to their anatomy, are more detectable.

No methods describing automatic detection of cervical vertebrae in fluoroscopic images have been found. Due to the fact that manual markings are laborious, the aim is to develop an automatic method for detection of the vertebral landmarks in the cervical spine, using fluoroscopic recordings. A prerequisite for the automatic detection method is a detection of the vertebral landmarks without the requirement of a large data set.

Chapter 3

Project aim

This chapter presents the object of this thesis along with specified assumptions.

3.1 Objective of project

The aim of this thesis is to develop a method for automatic detection of the cervical vertebrae in fluoroscopic images. The two ventral and two dorsal corner points of each vertebral body constitute the landmarks to be found. Due to the absence of a vertebral body in C1 and the anterior parts of C1 and C2 appearing as one, it is not included in the aim to automatically detect C1, and the landmarks of the cervical vertebra C2 are reduced to include only the inferior corners. The possible partial occlusion of C7 reduces the landmarks of this cervical vertebrae to include only the superior corners.
The objectives are to:

- Automatically localize the cervical vertebral bodies C3-C6 in a fluoroscopic image
- Automatically detect the four landmarks in each of the four localized vertebral bodies
- Automatically detect a minimum of the two inferior landmarks of C2
- Automatically detect a minimum of the two superior landmarks of C7
- Visually validate the automatic detection method

3.1.1 Assumptions

The videos used for automatic detection of the cervical vertebrae C3-C6 must be fluoroscopic recordings of a flexion movement or an extension movement in lateral view, with no physical restriction of the subject. The fluoroscopic recording begins with the subject in neutral position and ends with the cervical region in fully flexed or extended position. The cervical spine in the beginning of the recording is anticipated to be centered in the image. It is assumed that no axial rotation or lateral flexion occur and the vertebral bodies are regarded as rigid objects.

Chapter 4

Problem solution

This chapter comprises a description of the available data for the development of the automatic detection method, followed by a solution to the specified aim in Chapter 3*. The automatic detection method is divided into four main steps consisting of location of external markers, detection of C3-C6, detection of C2 and detection of C7. The chapter finalizes with a description of an applied optimization and the visual validation of the developed method.*

4.1 Data description

The fluoroscopic recordings were acquired using the Phillips BV Libra mobile diagnostic fluoroscopic image acquisition and viewing system. The system consisted of two main components: (1) the C-arm containing the camera, the image intensifier, the collimator and an X-ray tube; and (2) the mobile viewing station. Two separate videos were recorded for each subject; one from neutral position to full flexion of the neck; and one from neutral position to full extension of the neck. The RGB-videos were 576×768 pixels and recorded at a rate of 25 frames per second with a bit depth of 24. The subjects wore glasses with two metal balls on each side serving as external markers for the occiput (base of the skull). The external markers were used in another study [Plocharski et al., 2018], for the calculations of the angular motion between the base of the skull and C1. For the development of the automatic detection, eight videos of four different subjects performing flexion or extension of the cervical region were used. Frames with the subject in a neutral position were extracted, resulting in automatic detection of the vertebral bodies of C3-C6 and the inferior corners of C2 along with the superior corners of C7 for each fluoroscopic recording. An example of an image, where the automatic detection method should localize the vertebral bodies of C3-C6 and determine their four corners, along with the inferior corners of C2 and superior corners of C7 (marked by a red rectangle), is illustrated in *Figure 4.1.* The automatic detection method has been developed using MATLAB R2018a.

4.1.1 Frames used for development of the method

The development of the automatic detection method should satisfy the conditions of the objectives described in *Chapter 3*, where the only human interaction is the loading of the fluoroscopic video. The image to be loaded is an automatically extracted frame from the fluoroscopic recording with the subject in neutral position prior to a flexion or extension movement has started. Using a frame where the subject is yet to onset, the movement reduces the motion blur in the image and provides clearer edges of the vertebral bodies. *Figure 4.2* shows an example of image blurring due to motion during the fluoroscopic recording.

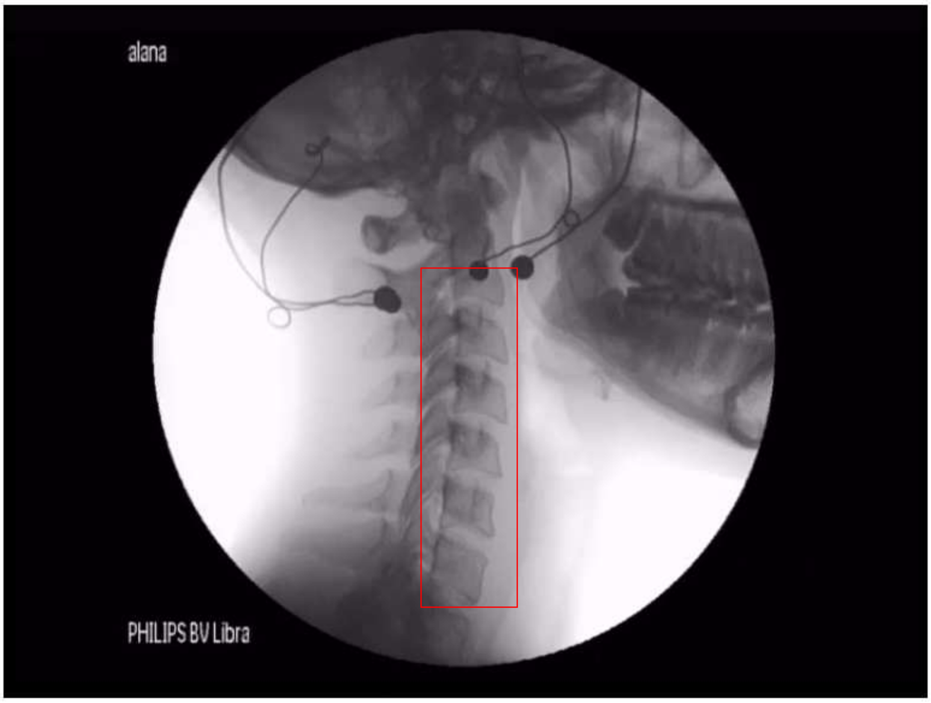

Figure 4.1: A fluoroscopic recording of a subject in neutral position prior to the onset of movement. The vertebral bodies of C2-C7, to be identified by the automatic detection method, are delineated by a red rectangle. The four external markers appear as dark circles.

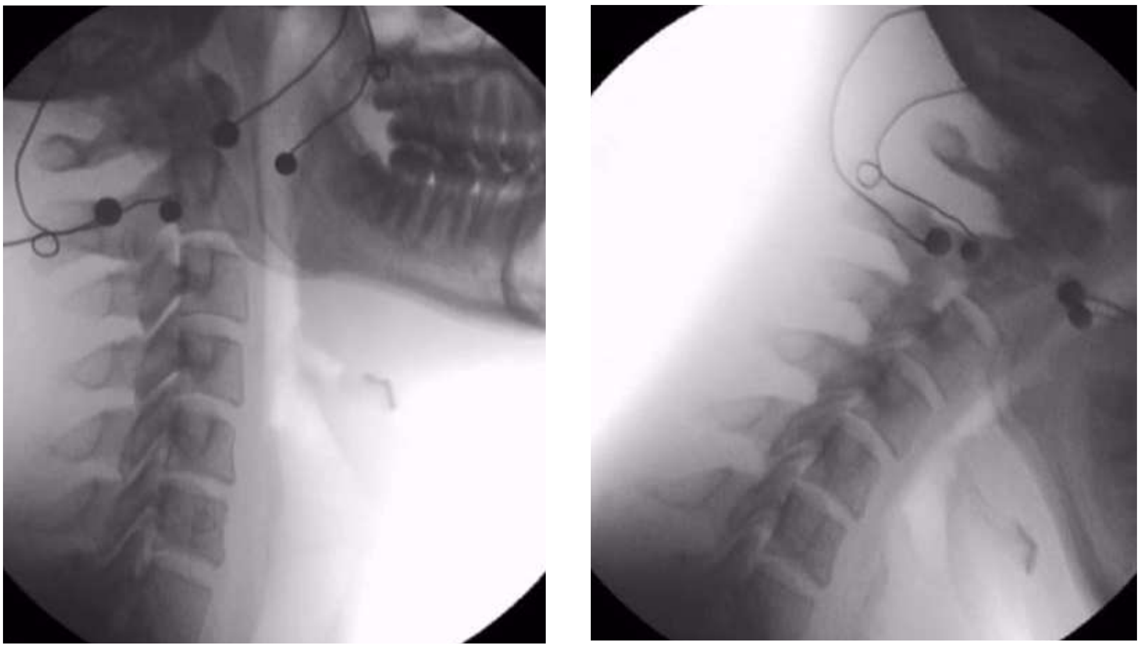

Figure 4.2: An example of motion blur during a fluoroscopic recording. To the left is an image of a subject in neutral position prior to the onset of a flexion movement, where the edges of the vertebral bodies are moderately easy to observe. To the right is an image of the same subject during the flexion movement, where particularly the ventral edges of C2, C3 and C4 are difficult to separate from the background due to motion blur.

In the fluoroscopic recordings, the subjects wore glasses with four metal balls to mark the occiput. These external markers can be used during tracking to calculate the angular motion between the occiput and C1; thus, an automatic detection of their center points are desirable.

4.2 Locate external markers in image

After the image is loaded, it is converted to a grayscale image, and the four external markers for the occiput are located. The external markers are circular, hence, the method used for their detection is a circular Hough transform-based algorithm.

The circular Hough transform detects objects with a radius within a specified range. The circular objects have three unknown parameters r (radius), a (center point in the x-direction), and b (center point in the y-direction) and these are identified during three steps. The first step is to threshold the grayscale image in order to identify all edges in the image. During the second step, all edge pixels are regarded as center of a temporary circle with a radius within the specified range. During the third step, the centers of the circles to be detected in the image are found. This is obtained by locating where the majority of the temporary circles intersect; thus, the intersection point constitutes the center of a circle in the image. [Pedersen, 2007]

The external markers have a radius between seven and 15 pixels, which specify the range of the radii for the temporary circles. A sensitivity factor between zero and one is specified and determines what can be regarded as circles in the image. A high sensitivity factor allows for weaker circular objects to be considered as circles and increases the risk of false detection. An image of all identified circular objects, delineated by blue circles, with a sensitivity factor of 0.98 and an edge gradient threshold of 0.09, is illustrated in *Figure 4.3*.

The circular Hough transform is robust to variations in illumination, image noise and partial occlusion. The latter is an advantage when the external markers partially overlap. The result of the identified circles, in addition to the centers and the radius, is a measure of the circle strength. The localization of the external markers is based on the intensity level and the entropy of the circles, and the center and radii of the four circles with the highest circle strength constitute the four external markers. An image of the four external markers located in the image is portrayed in *Figure 4.4*.

If the external markers are located on top of each other in the image, or the contrast between the marker and the background is too low to result in an edge from the thresholding, it results in a false detection. *Figure 4.5* presents an example of a false detection, where the two posterior markers are identified as one object, resulting in an external marker to be detected as part of the tooth.

4.3 Detection of vertebral bodies C3-C6

Before the corners of the vertebral bodies C3-C6 can be detected, the search is narrowed down for the localization of each vertebral body in the image by defining a region of interest (ROI). For the detection of the vertebral bodies C3-C6 in the image, a binary template is matched to a binarized version of the image. The detection process of the vertebral bodies C3-C6 is shown in the flowchart in *Figure 4.6*.

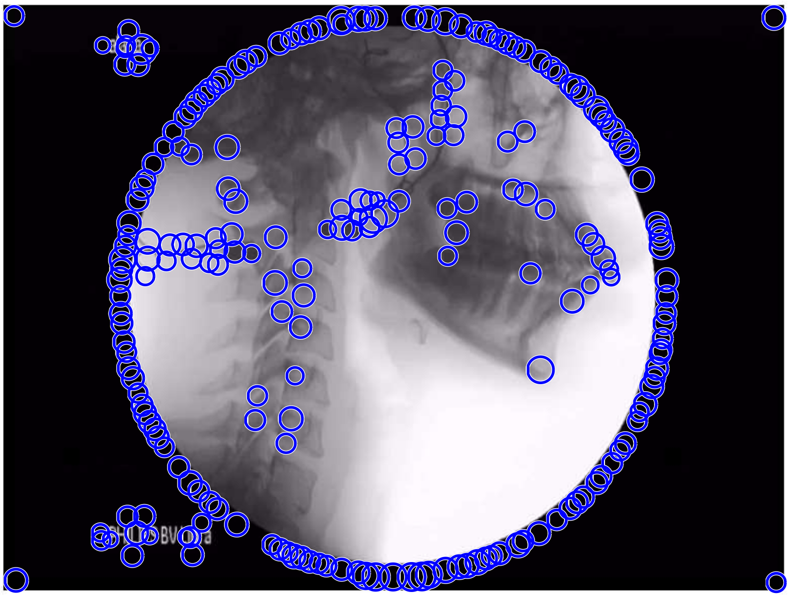

Figure 4.3: All circular objects with a radius between seven and 15, a sensitivity factor of 0.98 and an edge gradient threshold of 0.09 located by the circular Hough transform algorithm.

When the subject is in neutral position, the cervical spine is expected to be centered in the image. This allows for a creation of a ROI to narrow the search for the positions of the vertebral bodies in the image. The dimensions of the ROI are $\frac{1}{1.7}$ of the original image with the same ratio and center in the center of the original image. A local range filter is employed, and in order to locate the edges, a Canny edge detection algorithm is applied. The utilization of the Canny algorithm allows for a lower and upper threshold resulting in a higher robustness towards noise compared to other edge detection methods, and it is more likely to detect weak but true edges if they are connected to stronger edges. The lower threshold is 0.02 and the upper threshold is 0.05, as proposed by [Nøhr et al., 2017]. The result is a binary image containing both the inner and outer edge of the vertebral bodies. To fuse the inner and outer edges, a morphological closing is performed using a spherical structured element with a radius of two pixels. The results of the Canny edge detection and the morphological closing operation are shown in *Figure 4.7*.

To locate the vertebral bodies C3-C6 in the image, a binary template is constructed and matched to the binary image. The template is an image of 85-by-85 pixels. The background is black and the object is a white polygon with a seven pixels wide edge. The template is presented in *Figure 4.8*.

The template matching is conducted by calculating the Dice coefficient using a general sliding neighborhood operation with a window size equal to the size of the template. The Dice similarity coefficient [Dice, 1945], is often used as a statistical measure of the spatial overlap of a segmented image and its ground truth and is given by [Zou et al., 2004]:

$$DSC = \frac{2 \mid A \cap B \mid}{\mid A \mid + \mid B \mid}$$

where $\mid A \mid$ and $\mid B \mid$ denote the cardinalities or number of elements in each set and $\cap$

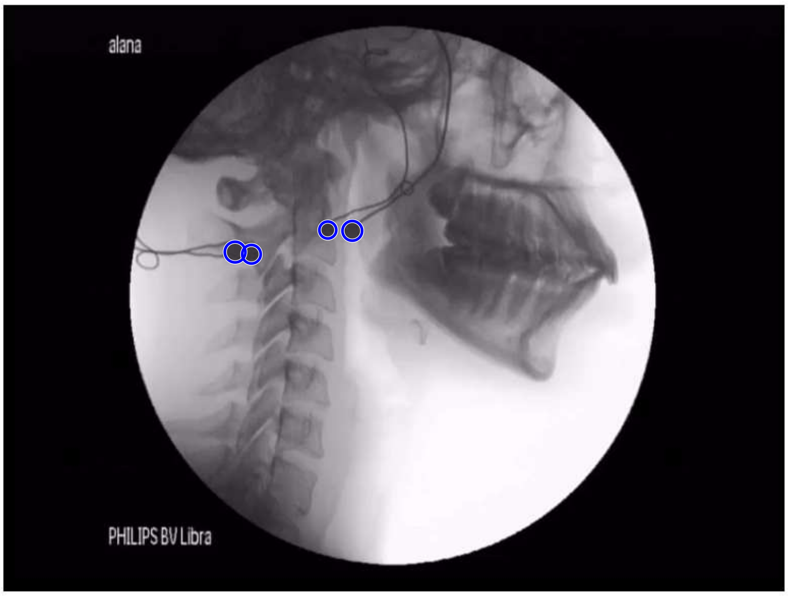

Figure 4.4: The four circles with highest circle strength after exclusion of circular objects based on intensity and entropy.

denotes the intersection. A DSC of zero means no spatial overlap, whereas a DSC of 1 is a complete overlap. In this case, the DSC is utilized to locate regions in the binary image similar to the template. The two images must be the same size and therefore the DSC is calculated for each sliding block of the binary image with the same dimensions as the template. The criteria for the possible locations are defined by a maximum number of 50 and a neighborhood size of 49-by-49 along with a $DSC \geq 0.34$. The DSC threshold is set low due to the different sizes and shapes of the vertebral bodies. An image of the locations that satisfy the criteria is shown in *Figure 4.9*. All possible locations are cropped, possessing the same dimensions as the template image and saved along with their respective center points.

Each possible location is evaluated in order to exclude false locations based on a range of criteria. The grayscale images of the true locations, have been found to possess average intensities in the range $100 - 150$. Images with an average intensity above or below the determined range are excluded from further processing. The remaining exclusion criteria are based on texture analysis. Local entropy describes the randomness in 9-by-9 neighborhoods of the image and for the evaluation of the possible locations, the mean value and the standard deviation are determined. The mean value is generally higher for the true locations compared to the false locations, and the ideal threshold for the true locations has been found to be > 1.99. The standard deviation of the local entropy is generally lower regarding the true locations and the threshold is determined to be < 1.14. The final evaluation of the locations is based on the properties of their respective gray-level co-occurrence matrix (GLCM). The GLCM estimates how frequently two horizontally adjacent pixels with certain intensity values occur, and the properties contrast, correlation, energy and homogeneity are used for evaluation of the locations. The contrast property is the intensity contrast or variance between a pixel and its neighbor over the entire image, and the threshold is determined to be in the range $0.045 - 0.12$. The correlation

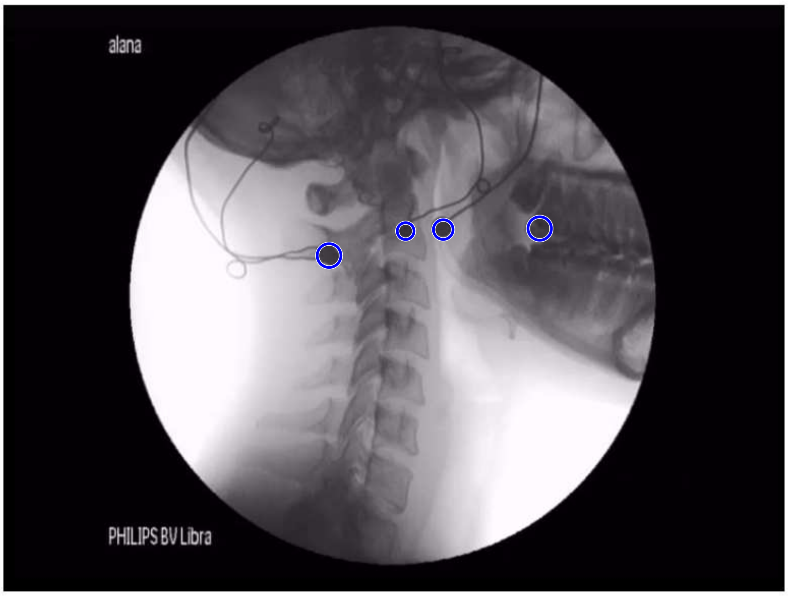

Figure 4.5: The two posterior external markers are located on top of each other, resulting in an identification as one object. This leads to a false identification of the fourth external marker, which is part of the subject's tooth.

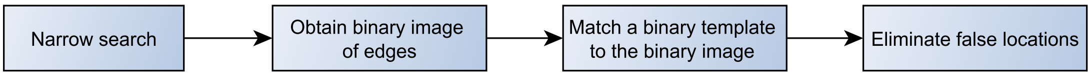

Figure 4.6: Flowchart showing the steps of the localization of the vertebral bodies C3-C6.

property describes the correlation between a pixel and its neighbor over the entire image and the range for the true locations is determined to be between $0.93 - 0.98$. The energy property is the sum of squared elements in the matrix and the range is determined to be $0.2 - 0.34$. The last evaluation criteria is the homogeneity property, which describes the closeness of the distribution of elements in the matrix to the diagonal, and the range is set to $0.94 - 0.98$. An image of the possible locations, after all the inclusion criteria are met, is shown in *Figure 4.10*.

The exclusion criteria are not able to eliminate all false locations, due to the varying intensities of the vertebral bodies and the fact that they do not uniquely differ from all the falsely detected locations. The candidate locations of the vertebral bodies are saved for processing in the final steps of the automatic detection method.

4.3.1 Segmentation of C3-C6

Each of the candidate locations are further processed as individual sub-images. A sub-image is loaded and the edge of the vertebral body is detected. If the detected edge is not a vertebral body, it is presumed to be a false location, and is excluded. The four corners of a vertebral body are located and finally the corner points are transferred to the original frame from the fluoroscopic recording. The corner detection process is illustrated in the flowchart in *Figure 4.11*.

Figure 4.7: To the left is an image of the applied Canny edge detection algorithm, with a lower threshold of 0.02 and an upper threshold of 0.05, results in a binary image containing the inner and the outer edges of the objects in the image. To the right is the final binary image after a morphological closing operation.

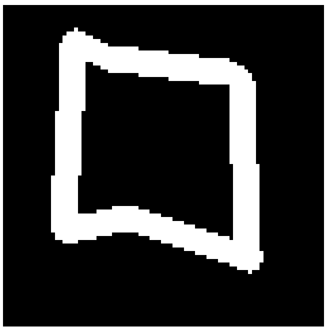

Figure 4.8: The template to be matched to the binary image.

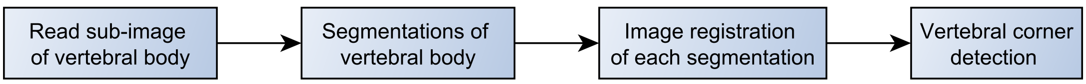

Figure 4.11: Flowchart showing the steps of the corner detection process performed for each of the vertebral body locations.

After the sub-image has been loaded, it is processed to enhance the edges in order to perform segmentation of the vertebral body. The edge enhancement is obtained by conducting a power-law transformation. The power-law transformation is defined as [Vimal and Thiruvikraman, 2012]:

$$s = cr^{\gamma}$$

where s is the gray-levels of the output pixels, r is the gray-levels of the pixels in the input image and c is a constant. By visual inspection, the values are determined for $c = 1$ and $\gamma = 1.1$ for the contrast enhancement. After the power-law transformation, an

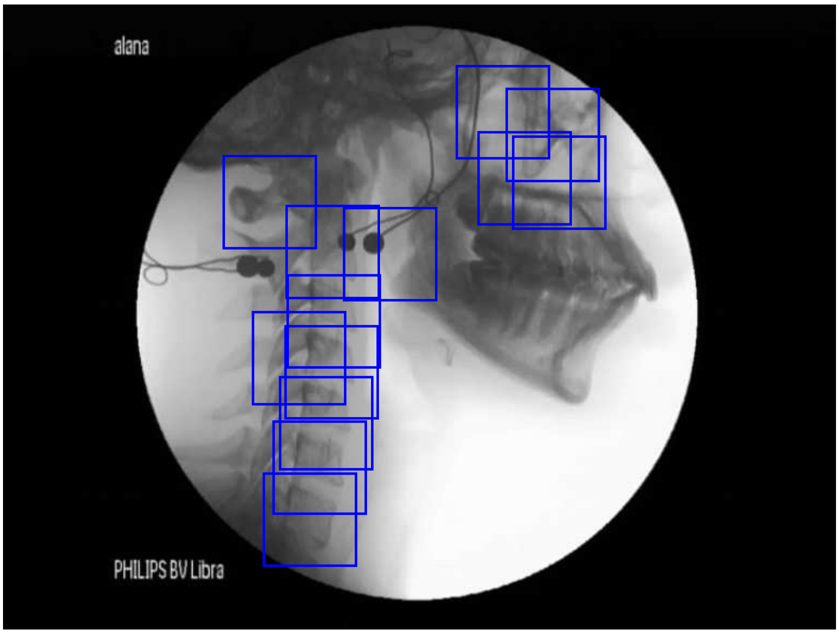

Figure 4.9: Image of all the locations that satisfy the criteria of the local maxima object.

anisotropic diffusion filter is applied to reduce the noise within the image, while preserving the sharpness of the edges [Perona and Malik, 1990]. The optimal gradient threshold is automatically estimated based on the individual sub-image. An example of a grayscale sub-image is shown in *Figure 4.12* along with the result of the power-law transformation and the applied anisotropic diffusion filter.

For the edge detection of the vertebral bodies, a single method has not been found optimal for all the sub-images. To solve this problem, a multi-segmentation approach is utilized, where different segmentations are conducted on each sub-image in order to remove false edges and solely obtain the edge of the vertebral body. The segmentations include further enhancements, filtering and different morphological operations among other things.

After the anisotropic diffusion filtering of a sub-image, the segmentations utilize two main methods. The first method applies a contrast-limited adaptive histogram equalization algorithm before it separates into three secondary segmentation approaches. The second method for the segmentations initializes with the gradient magnitude of the filtered sub-image.

Segmentation: Method 1

A contrast-limited adaptive histogram equalization (CLAHE) algorithm is used to enhance the contrast in the grayscale sub-image. The algorithm works on small regions of the image by examining the histogram of intensities in the region [Pizer et al., 1990]. The segmentation *Method 1* divides intro three segmentation approaches: **Method 1a**, **1b** and **1c** as elaborated on below.

Method 1a

The first segmentation approach of *Method 1* applies a sharpening of the sub-image to

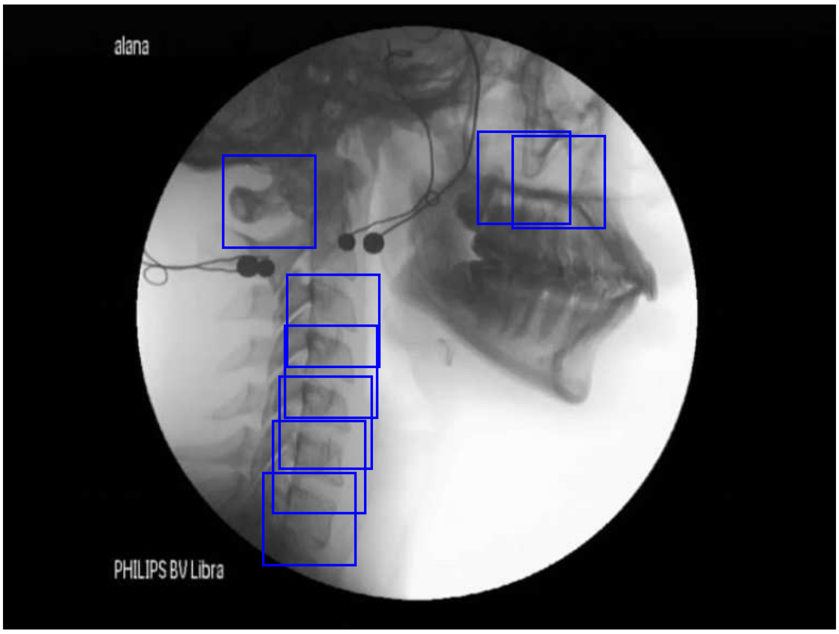

Figure 4.10: Image of the possible locations of the vertebral bodies after the exclusion of false locations based on intensity, entropy and properties of the gray-level co-occurrence matrix.

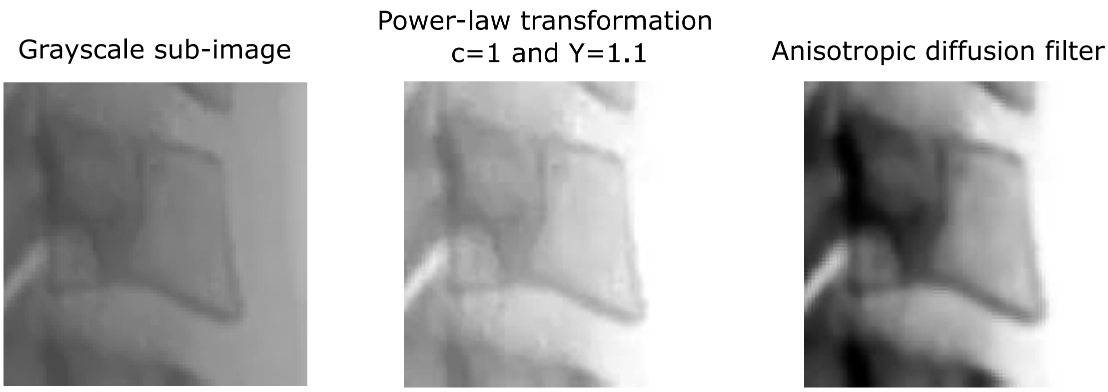

Figure 4.12: Edge-preserving contrast enhancement of a grayscale sub-image shown to the left. In the middle is the result of the power-law transformation and to the right is the result of the anisotropic diffusion filter.

enhance the contrast along the edges, using a standard deviation of the Gaussian lowpass filter value of 3 and a sharpening effect strength of 2. After the sharpening, an adaptive threshold is applied to 3-by-3 blocks of the sub-image to filter noise while preserving the edges. A gray-level co-occurrence matrix is calculated to obtain information about the texture in the image. Yet again, an adaptive threshold is applied to 3-by-3 blocks, and the resulting image is processed in two ways.

During the first processing, the image is binarized with a threshold of 0.99 and any holes inside the objects in the image are filled. During the second processing of the resulting image, a fourth order Butterworth bandpass filter is applied with a lower cut off frequency of 5 and a higher cut off frequency of 71 [Teyhen et al., 2007]. The resulting image contains added noise and to remove this, the image is binarized with $t = 0.99$ and objects are filled before it is fused with the first binary image. The result of the fusing is an image where a pixel is white if and only if it was white in both images. In order to remove edges that do not belong to the vertebral body, a mask is applied to the image to set any pixel outside the mask to zero. The mask is the template image where the edge is dilated with a spherical morphological structuring element with a radius of 3 (SE3) and the object is filled.

The remaining operations in this approach include selecting the largest connected component in the image and several morphological operations. Morphological opening, closing, erosion and dilation are specified with a spherical structuring element with a radius between 1 and 5 (SE1-SE5), bridging is utilized for connecting components in the image that are one pixel apart, and, finally, a morphological operation that removes all interior pixels, leaving only the border. The only difference between the segmentations utilizing **Method 1a**, which is shown in the flowchart in *Figure 4.13*, is an added morphological opening with SE5 in one of them, before the border of the object is found.

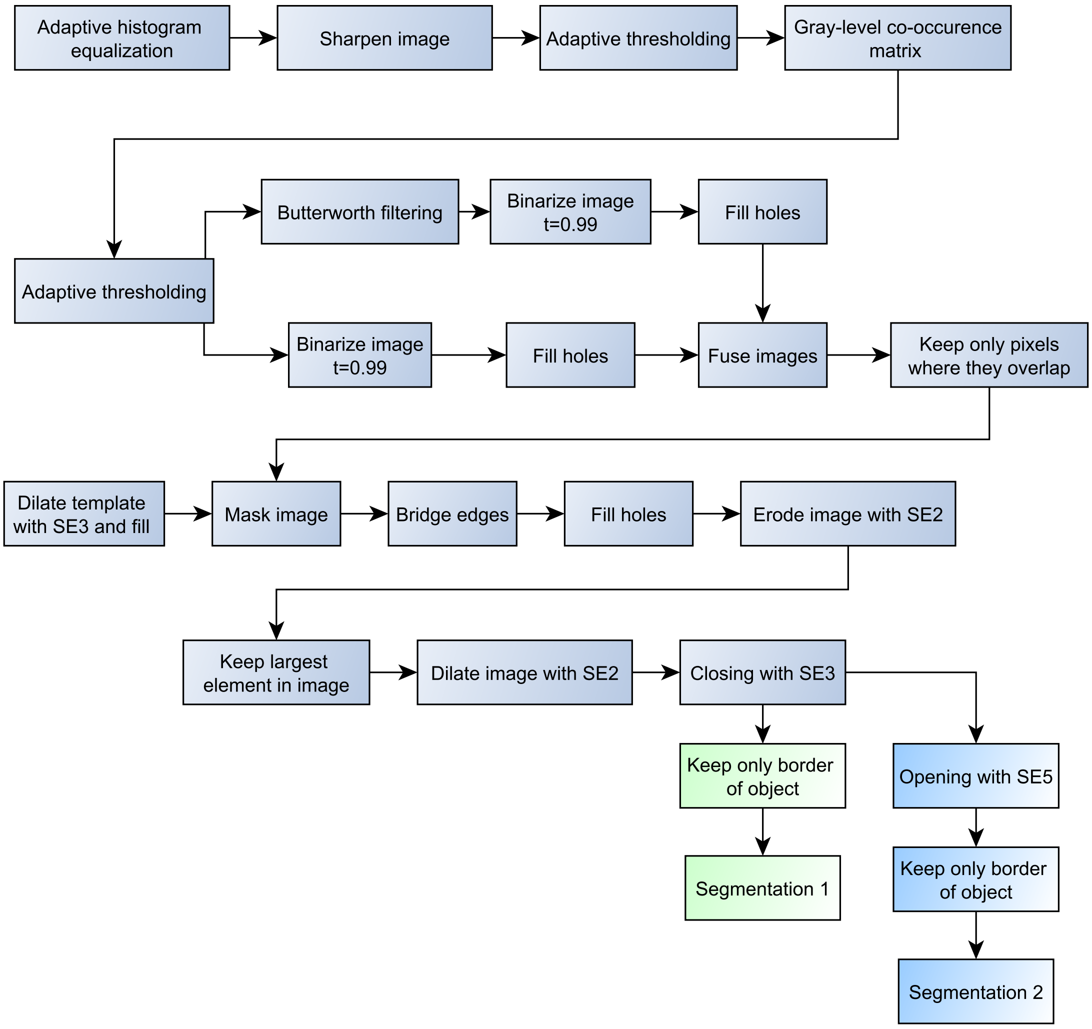

Figure 4.13: A flowchart showing the segmentation approach 1a of the main *Method 1*.

Method 1b

The second segmentation approach of *Method 1* applies edge detection on the CLAHE image, using the Canny method with a lower threshold of 0.02 and an upper threshold of 0.05 [Nøhr et al., 2017]. The Canny edge image is the basis for the majority of the segmentations in the multi-segmentation approach. Morphological operations, selection of largest element and removal of connected components smaller than a specified size are utilized in different orders for the segmentations. Different modifications of the template image are used as masks as in **Method 1a**, and in one case the template object is modified to be 8 pixels lower than the original, before a morphological dilation with a SE3 is applied. For all segmentations the border of the object is found. A flowchart of the segmentations utilizing **Method 1b** is illustrated in *Figure 4.14*.

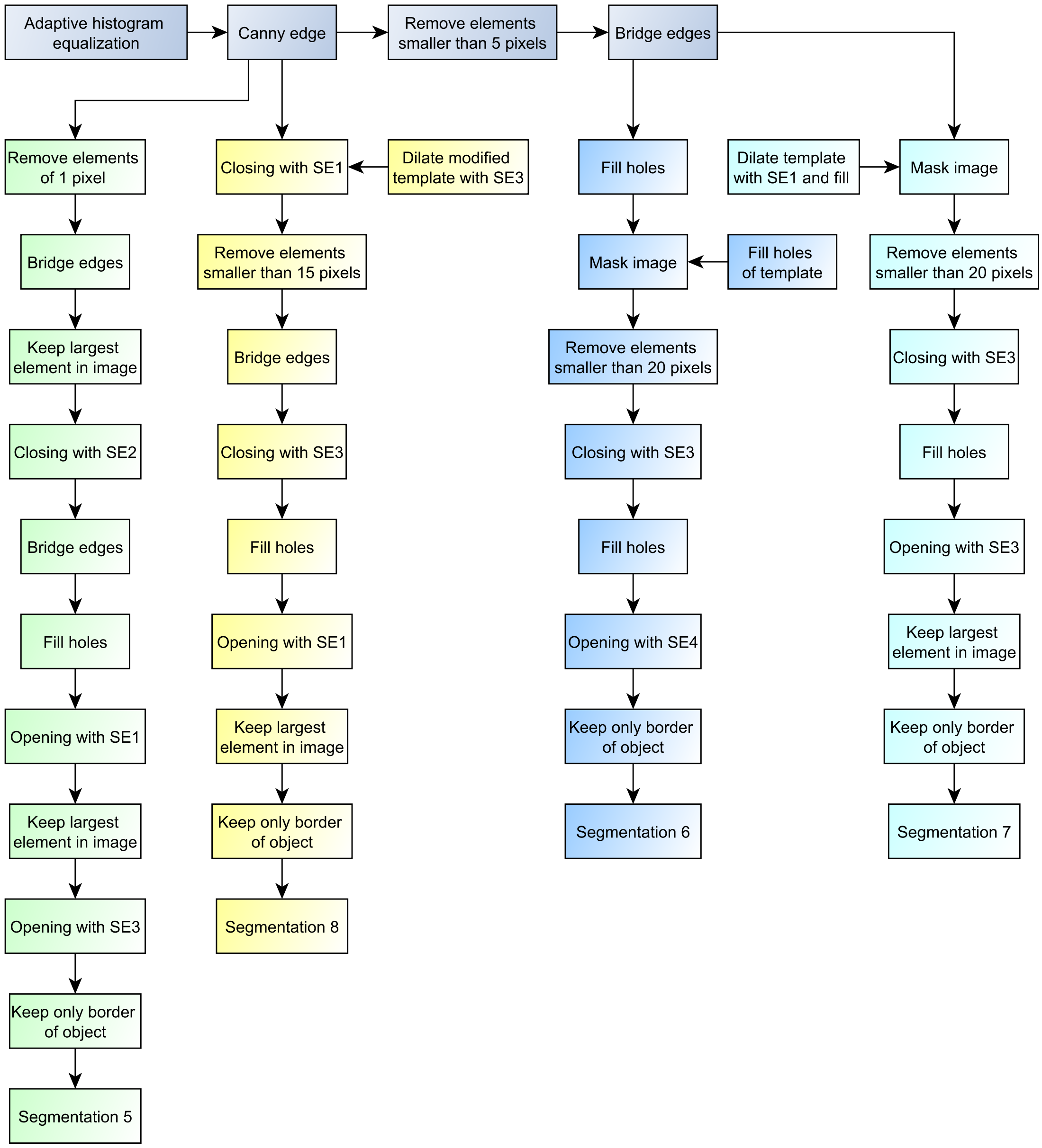

Figure 4.14: A flowchart showing the segmentation approach 1b of the main *Method 1*.

Method 1c

The third segmentation approach of *Method 1* utilizes a fusion of three different edge detections, using the Canny method all with the same threshold values as in **Method 1b**. The first Canny edge image is the same as the one utilized in **Method 1b**. The remaining two Canny edge images are obtained from the first and second adaptive thresholding techniques from **Method 1a**. The resulting fused image contains all edges from the three Canny edge images. The image is binarized with a threshold of 0.01, and different orders of morphological operations and largest object selection constitute different segmentations before the border of the object is identified. A flowchart of the segmentations utilizing **Method 1c** is listed in *Figure 4.15*.

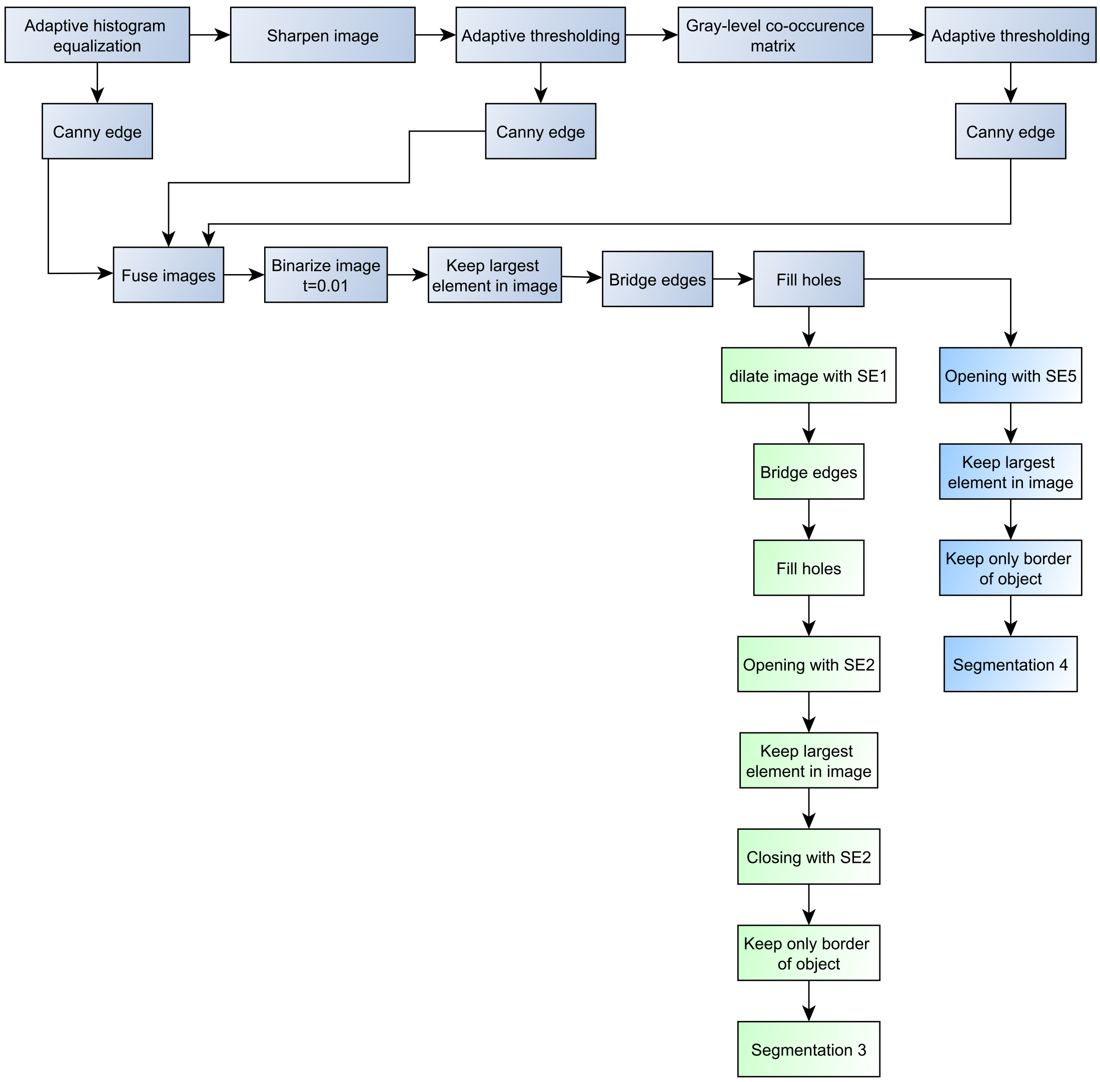

Figure 4.15: A flowchart showing the segmentation approach 1c of the main *Method 1*.

Segmentation: Method 2

The second method applies the gradient magnitude on the anisotropic diffusion filtered image. The gradient magnitude image is filtered using an edge-preserving fast local Laplacian filter, with $\sigma = 0.9$, which characterizes the amplitude of the edges and $\alpha = 0.1$, which controls the smoothing of details [Aubry et al., 2014]. The sub-image is sharpened to enhance the contrast along the edges, using a standard deviation of the Gaussian lowpass filter value of 3 and a sharpening effect strength of 2. Adaptive thresholding is applied to obtain a binary image, where the local threshold is determined with the local median of the neighborhood and a maximum sensitivity of 1.

Different orders of morphological operations and largest object selection constitute different segmentations before the border of the object is identified. A flowchart of the segmentations utilizing *Method 2* is shown in *Figure 4.16*.

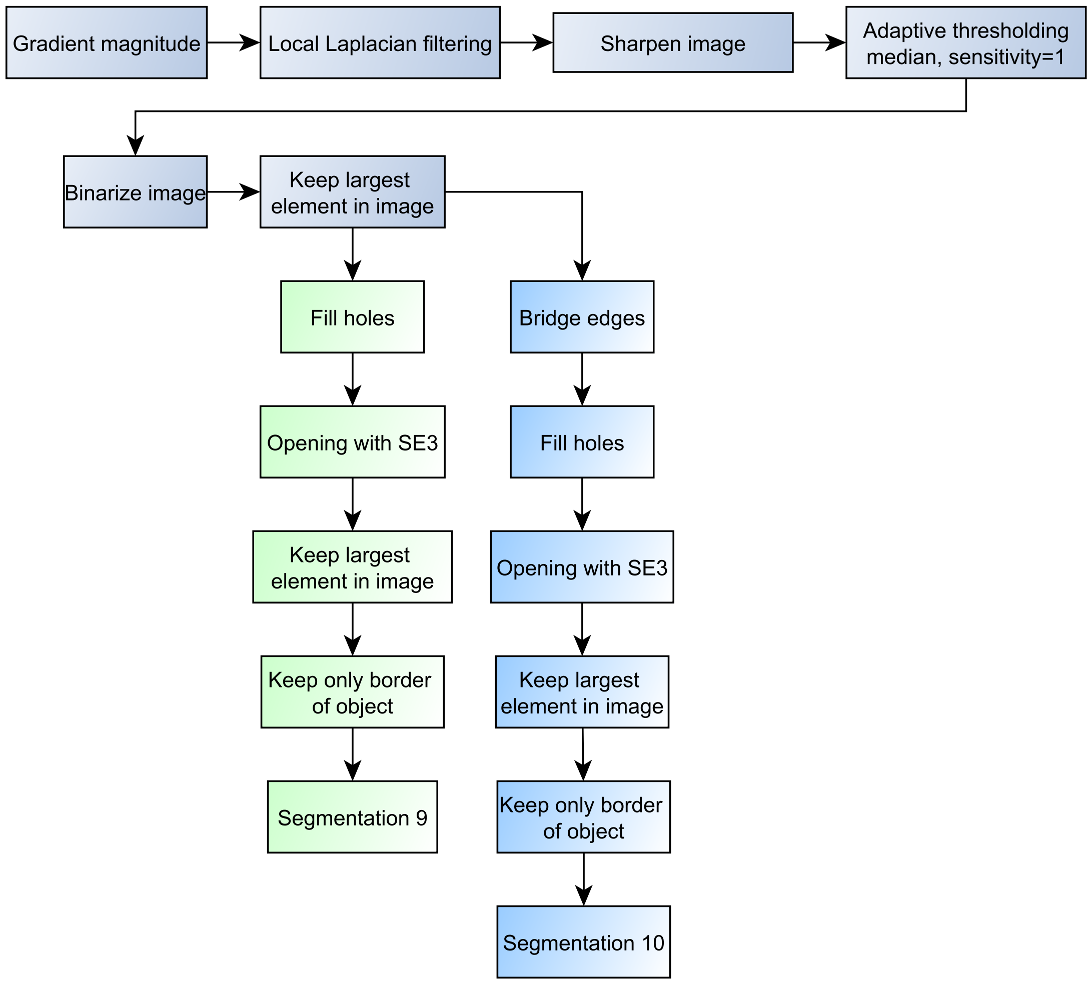

Figure 4.16: A flowchart showing the segmentation approach of the main *Method 2*.

The results of the multiple segmentations of a single sub-image containing a vertebral body are illustrated in *Figure 4.17*, where it is revealed that the best result is obtained by *Segmentation 2*.

4.3.2 Image registration

In order to determine which one of the multiple segmentations to apply to a sub-image, an automatic estimation of the quality of each segmentation is employed to decide which is preferable. No connection between the sub-image of a specific vertebra and which segmentation to employ has been found, and the best segmentation can even differentiate between sub-images of the same vertebral body in two subsequent frames.

To automatically estimate the best of the multiple segmentations for each sub-image, a registration is conducted for each segmentation. The registration requires two images of the same size; one fixed, and one moving. The moving image is transformed, using an affine transformation, consisting of translation, rotation, scale and shear to align with the fixed image. The moving image is the binary template image and the fixed image is the morphological dilation, with SE3 of the border object from each of the segmentations, resulting in as many registrations as the number of segmentations.

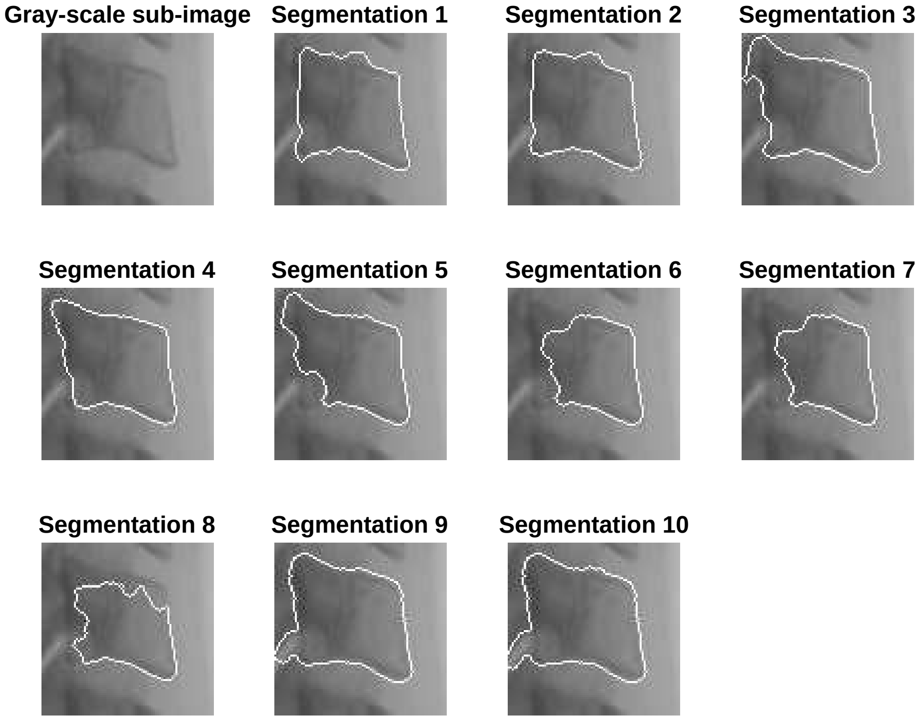

Figure 4.17: The results of the multiple segmentations of a vertebral body.

The metric to be optimized during the registration is the mean squared error and the optimizer is a regular step gradient descent optimization configuration, where the initial step length is 0.01 and the maximum number of iterations is set to 1000. The resulting transformed templates are evaluated by calculating the Dice coefficient of their corresponding fixed image, providing a measure of the quality of each segmentation obtained in *Section 4.3.1*. The segmentation resulting in the highest overlap with the transformed template image from the registration, thus producing the highest Dice, is selected as the best segmentation. The results of the registrations along with their corresponding calculated Dice value, are illustrated in *Figure 4.18*.

Due to the fact that not all of the false locations are eliminated at this point, any selected segmentation below the Dice value 0.72 is not considered a vertebral body and is, thus, excluded. Any segmentation, where the height exceeds the width plus an additional 10 pixels, is also excluded. The Dice threshold and the requirements of the dimensions result in further elimination of the false locations, however, not always all of them. The remaining sub-images are assumed to be the vertebral bodies and their corners are located.

4.3.3 Vertebral corner detection

The best segmentations of the remaining images are assumed to be the edges of the vertebral bodies C3-C6 and the four corners are located. The Euclidean distance between any pixel pair in the sub-image is calculated. The maximum distance, where the line inbetween constitutes a positive slope and the same where the line constitutes a negative slope are determined. The endpoints of the two maximum distance lines are presumed to be the four corners of the vertebral body. Knowing that the vertebral bodies are aligned at

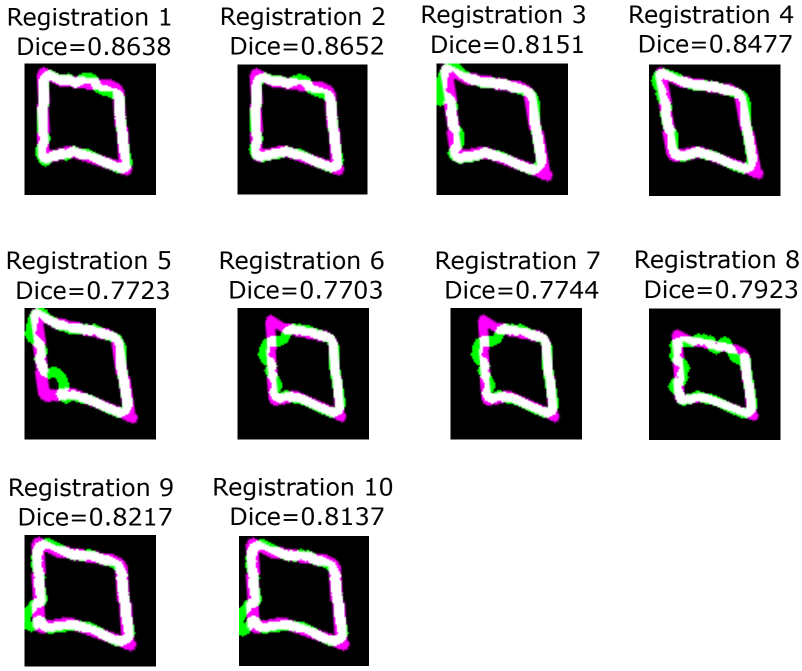

Figure 4.18: The results of the multiple registrations of the vertebral body shown in 4.17. The segmentation is green and the transformed template is magenta while the overlap is white. Based on the calculated Dice, *Registration 2* is estimated to be the best and the result from *Segmentation 2* is used for the corner detection of the vertebral body.

an approximately straight line, any remaining false locations are removed if they are more than half the width of the template image away from the true vertebral locations. The coordinates of the points are transferred to the original image along with the delineations of the external markers.

4.4 Detection of the inferior corners of C2

Due to the anatomical shape of C2, the superior corners of the vertebral body are not always detectable. The vertebral body of C2 can be detected in the image and the multi-segmentation approach might result in a border object that allows for the detection of the corners, but most often C2 is not detected by the template matching and multiple segmentations. To determine the location of the inferior corner points of C2, the known location of C3 is used. The center point of the C2 sub-image is estimated to be on the top border of the C3 sub-image and directly above the center point of C3. Due to the fact that the detection is limited to the inferior corners of C2, the height of the C2 sub-image is only 3/4 the height of the C3 sub-image but the same width. The C2 image is filtered using the power-law transformation and the contrast is enhanced before the ansisotropic diffusion filter is applied. The CLAHE algorithm is utilized and followed by a sharpening, and, finally, an adaptive threshold is applied to 3-by-3 blocks of the sub-image. These steps are identical to the initial steps described in *Section 4.3.1 (Method 1a)*.

After the image filtering, a morphological erosion is applied with a linear structuring element spanning a length of 4 pixels and an angle of 180°. Edge detection using the Canny method is followed by a morphological dilation with SE1 before the image is filtered to contain only the largest object and the holes inside the object is filled. The border of the object is constructed and the maximum Euclidean distance is calculated as in *Section 4.3.3*. Only the coordinates of the inferior corner points of C2 are transferred to the original image.

4.5 Detection of the superior corners of C7

As for C2, the vertebral corner points of C7 are not always detectable due to the potential partial occlusion of the inferior part of the vertebral body. For several frames, the C7 is detected during the template matching and satisfying segmentations result in detection of all four corner points of C7. For the frames, where all four corner points of C7 are not detected, the superior corners are subsequently detected based on the known location of C6. The center point of the C7 sub-image is estimated to be on the bottom line of the C6 sub-image and directly below the center point of C6. The dimensions of the C7 sub-image are similar to the sub-image of C2, and the filtering and processing of the image are identical to the steps used for C2 including the Canny edge detection.

After the edge detection using the Canny method, morphological bridging is utilized before anything but the largest connected component is removed. For the remaining element a morphological dilation with SE1 is applied, and holes inside the object are filled. Finally, an opening with SE5 is utilized before the border of the object is used for the calculation of the maximum Euclidean distance, where only the coordinates of the superior corner points are transferred to the original image.

4.6 Optimization and visual validation

In case of one or more of the vertebral bodies C3-C6 not being detected neither by the template matching nor due to the segmentations not revealing satisfying results, the next frame in the fluoroscopic recording is read and the automatic detection method is launched once more. When C3-C6 is found, and if C2 or C7 have not been detected, the inferior corners of C2 and the superior corners of C7 are found, based on the known locations of C3 and C6, respectively. To simplify the recognition of each detected vertebra, the corner points of C2 are blue, C3 are green, C4 are yellow, C5 are red, C6 are cyan and the corner points of C7 are magenta.

The validation is based on visual inspection of the plotted corner points of C2-C7 and delineation of the external markers. An automatic detection, leading to four corner points of C2 or C7, is the result of a detection using the multi-segmentation approach, while two corner points are the result of the subsequent segmentation of C2 or C7.

Chapter 5

Results

In this chapter, the results of the automatic detection method is described. An image from each of the eight fluoroscopic recordings showing the results of the method is presented.

5.1 Automatic detection method

The results of the automatic detection of the external markers and C2-C7 are represented by a frame from each of the eight fluoroscopic recordings. Furthermore, *Fluoroscopic recording 2* also illuminates the difference between the results of the automatic detection method in two subsequent images.

The automatic detection method has been tested on the initial five frames of each fluoroscopic recording, resulting in a total of 40 evaluated frames, and the method was able to correctly detect all four external markers in 27 frames. The method automatically detected C2-C7 in 31 of the 40 tested frames. In eight of the remaining tested frames, either one of the vertebral bodies C3-C6 was detected twice, resulting in an undetected vertebral body, or the detected vertebrae was falsely identified, leading C3 to be detected as C2, C4 to be detected as C3 and so on. Only in one case, the method was unable to detect sufficient vertebral bodies in the frame and resulted in automatic detection of the subsequent frame in the fluoroscopic recording.

The duration of the automatic vertebral detection ranged from 2 minutes and 38 seconds to 6 minutes and 48 seconds. The average duration of the 40 tested frames was 4 minutes and 13 seconds. The evaluation of the results is based on the visual validation conducted on each resulting image.

Fluoroscopic recording 1

The result of a frame in the first fluoroscopic recording is illustrated in *Figure 5.1*, where it is revealed that only three of the external markers have been detected correctly. The fourth external marker is occluded by one of the detected external markers. This has caused a tooth to be incorrectly detected as an external marker. In neither of the five tested frames, were all four external markers were correctly identified.

The automatic detection method was able to detect C2-C7 in three of the five tested frames. In one case, an insufficient quantity of vertebrae was detected resulting in the method to automatically proceed to the subsequent frame. The average duration of the five tested frames in *Fluoroscopic recording 1* was 4 minutes and 33 seconds.

The corner points of C7 have been detected through the multi-segmentation approach, where particularly the ventral points are found quite successfully. Generally, the ventral corner points for all vertebral bodies and all corner points of C4 and C5, except C2, have been detected rather precisely.

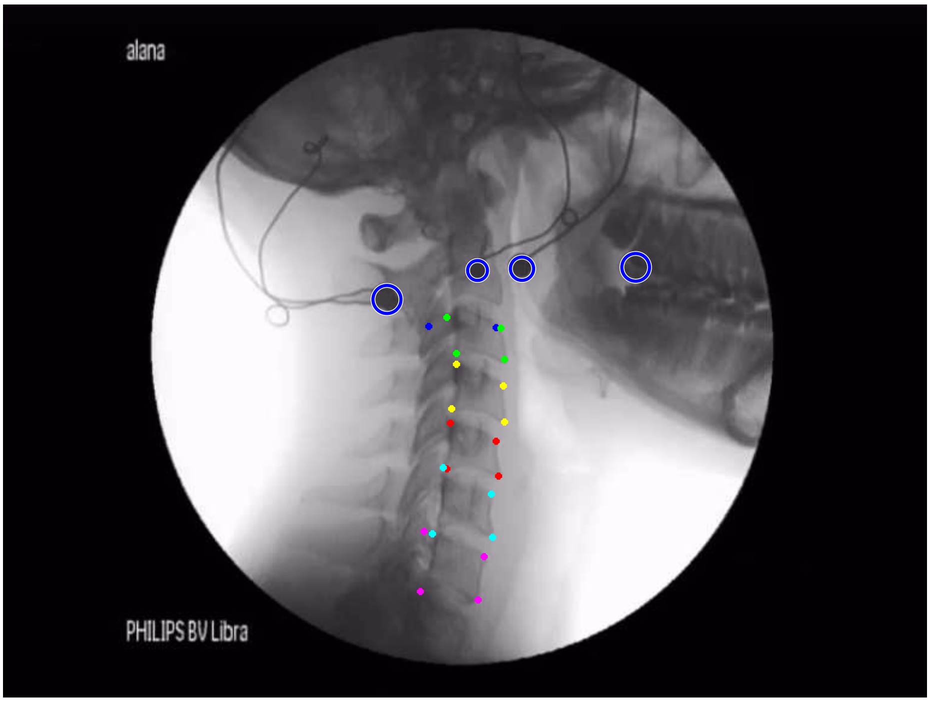

Figure 5.1: The result of the automatic detection method for *Fluoroscopic recording 1* with the vertebral corner points of C2-C7 and delineated external markers. As two of the external markers are located on top of each other, the detection has resulted in a false detection of the fourth marker.

Fluoroscopic recording 2

The result of a frame in the second fluoroscopic recording is illustrated in *Figure 5.2*, with all four external markers delineated. The external markers were detected accurately in all the tested frames.

The automatic detection of C2-C7 was only successful in two of the five tested frames, but these two also had the most precise detected corners, based on the visual validation. The *Fluoroscopic recording 2* had the longest average duration of 4 minutes and 59 seconds.

In the two frames where the detection was successful, C7 was detected through the multi-segmentation approach, while C2 was detected in one, using this method.

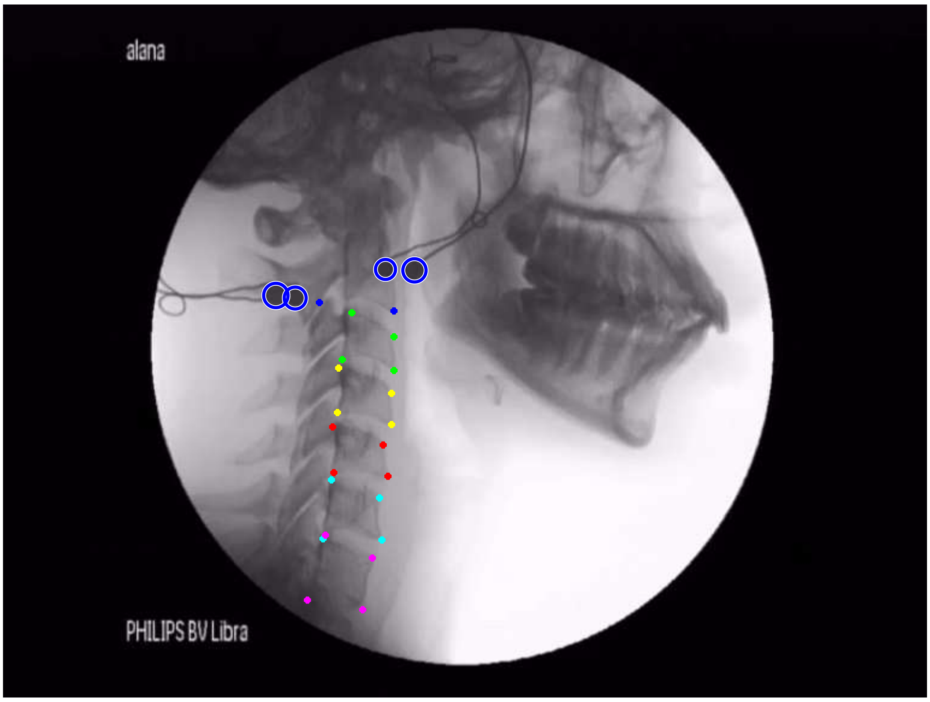

Figure 5.2: The result of the automatic detection method for *Fluoroscopic recording 2* with the vertebral corner points of C2-C7 and delineated external markers.

In *Figure 5.3* and *5.4*, the results of the automatic detection method from two successive frames are illustrated. In *5.3*, all vertebral bodies C2-C7 have been found using the multi-segmentation approach with a satisfying result. In *5.4*, only one frame later, the vertebral body C5 has been detected twice, resulting in C3 to be detected as C2 and C4 to be detected as C3 and C2 to not be detected at all.

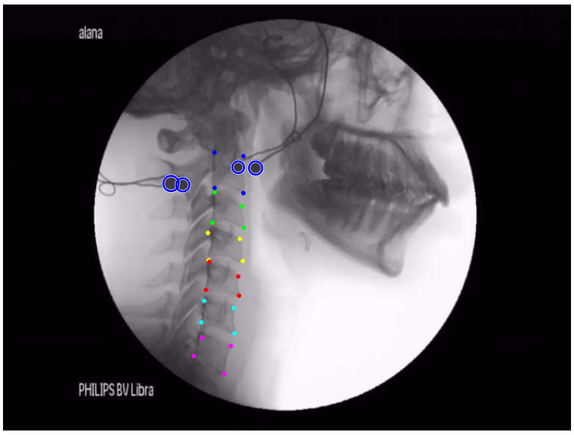

Figure 5.3: The result of the automatic detection method for *Fluoroscopic recording 2*, two frames after 5.2, with the vertebral corner points of C2-C7 and delineated external markers.

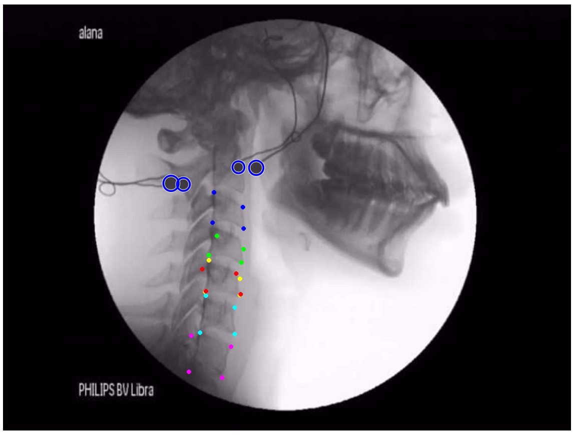

Figure 5.4: The result of the automatic detection method for *Fluoroscopic recording 2*, one frame after 5.3, with the estimated corner points of C2-C7 and delineated external markers.

Fluoroscopic recording 3

In *Figure 5.5*, the result of a frame in the third fluoroscopic recording is presented. All four external markers have been correctly detected although the two most dorsal external markers slightly overlap. In three of the five tested frames, the external markers were not identified correctly.

The detection of the inferior corners of C2 is inadequate, and it is seen that the ventral point is located at the edge of the mandible. The inferior corner points of C3 are inaccurate and the detection of the superior dorsal corner point of C6 has resulted in approximately the same point as the inferior dorsal corner point of C5. For the detection of the superior corner points of C7, particularly the ventral point is inaccurately detected. The remaining points, including all four corner points of C4 and C5, are visually very close to the true corner points.

The automatic detection method successfully located the vertebrae C2-C7 in all five of the tested frames, with an average duration of 3 minutes and 52 seconds.

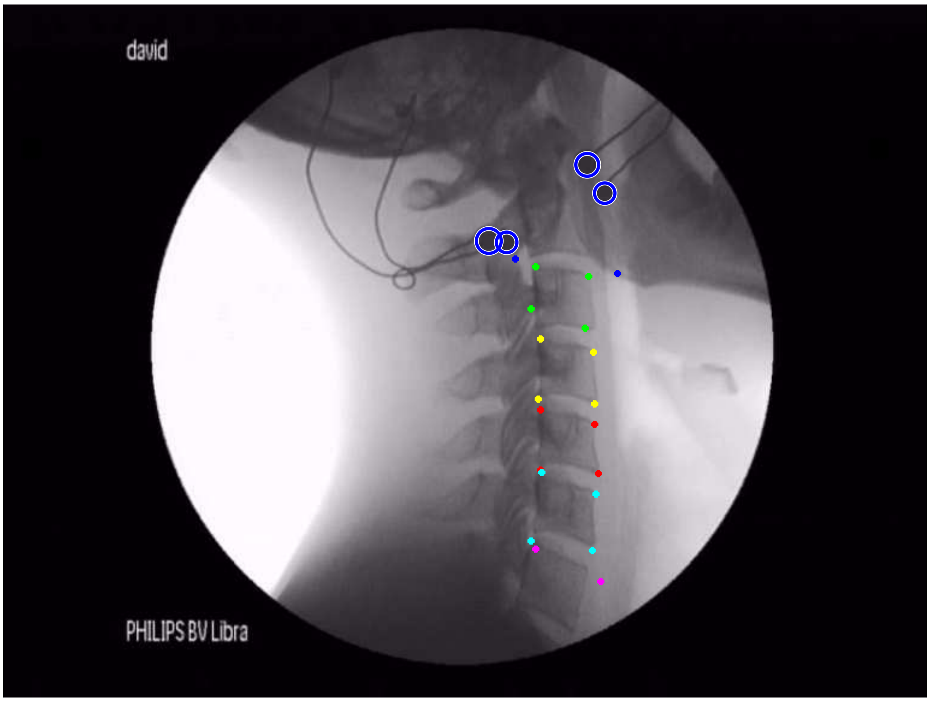

Figure 5.5: The result of the automatic detection method for fluoroscopic recording 3 with the vertebral corner points of C2-C7 and delineated external markers.

Fluoroscopic recording 4

A result of the fourth fluoroscopic recording is presented in *Figure 5.6* with correctly detected external markers, which was only the case in two of the five tested frames.

As in *Fluoroscopic recording 3*, the inferior corners of C2 are deviant, and the ventral corner point is located at the edge of the mandible. For the detection of the remaining vertebral corners, it is generally the ventral points that have been detected with greatest accuracy.

The cervical vertebrae C2-C7 was successfully located in three of the five tested frames. The average duration of the automatic detection method to locate the corner points of the cervical vertebrae in a frame spanned 3 minutes and 43 seconds.

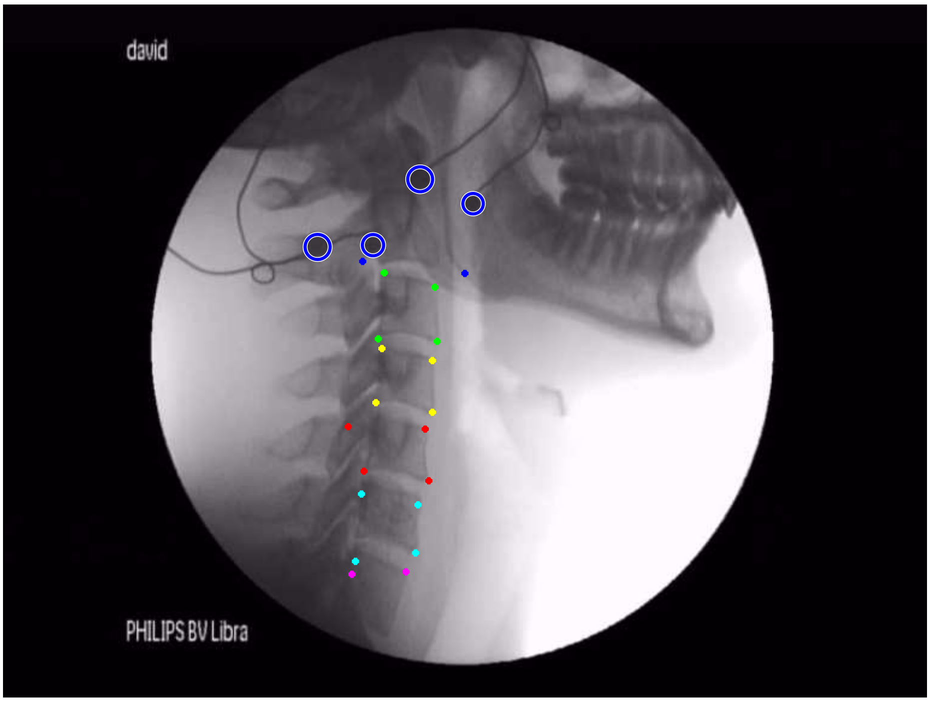

Figure 5.6: The result of the automatic detection method for *Fluoroscopic recording 4* with the vertebral corner points of C2-C7 and delineated external markers.

Fluoroscopic recording 5

Figure 5.7 shows the result of a frame in the fifth fluoroscopic recording. All four external markers have been correctly detected. In two of the five tested frames, one of the external markers was not identified accurately.

In general, the located corner points are quite accurately detected. The estimated inferior corners of C2 have resulted in two false locations, where the detected ventral corner point and the true corner have similar intensities. Again, the highest precision is generally achieved with the ventral corner points, detected within a few pixels of their respective true corner.

Of the five tested frames, four were successful and the average duration of the automatic detection method lasted 3 minutes and 36 seconds for the five frames.

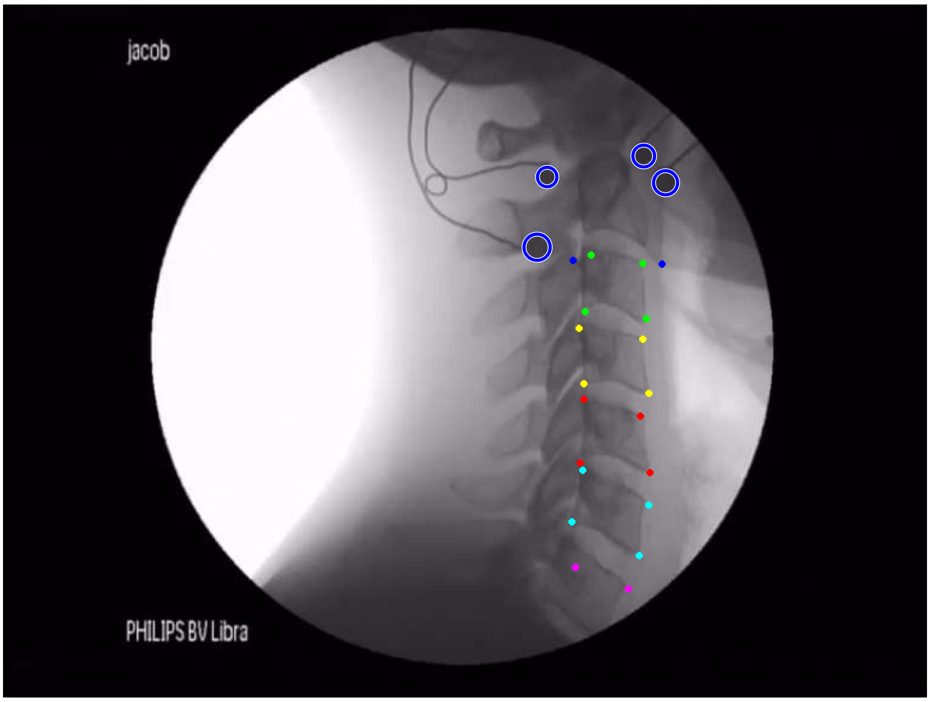

Figure 5.7: The result of the automatic detection method for *Fluoroscopic recording 5* with the vertebral corner points of C2-C7 and delineated external markers.

Fluoroscopic recording 6

For the sixth fluoroscopic recording, the result of a frame is revealed in *Figure 5.8*, where all external markers are correctly delineated in all tested frames, although the markers overlapped in pairs.

The corner points of C2 are located through the multi-segmentation approach, but all four of the detected points are quite far from the true corners of C2. The detected corner points of C6 are off target, but in general it is the detection of C2 and C7 that appear most inaccurate.

As in *Fluoroscopic recording 5*, four of the five frames resulted in successful detection of C2-C7. The average duration was 4 minutes and 44 seconds, which was the second longest duration of the fluoroscopic recordings.

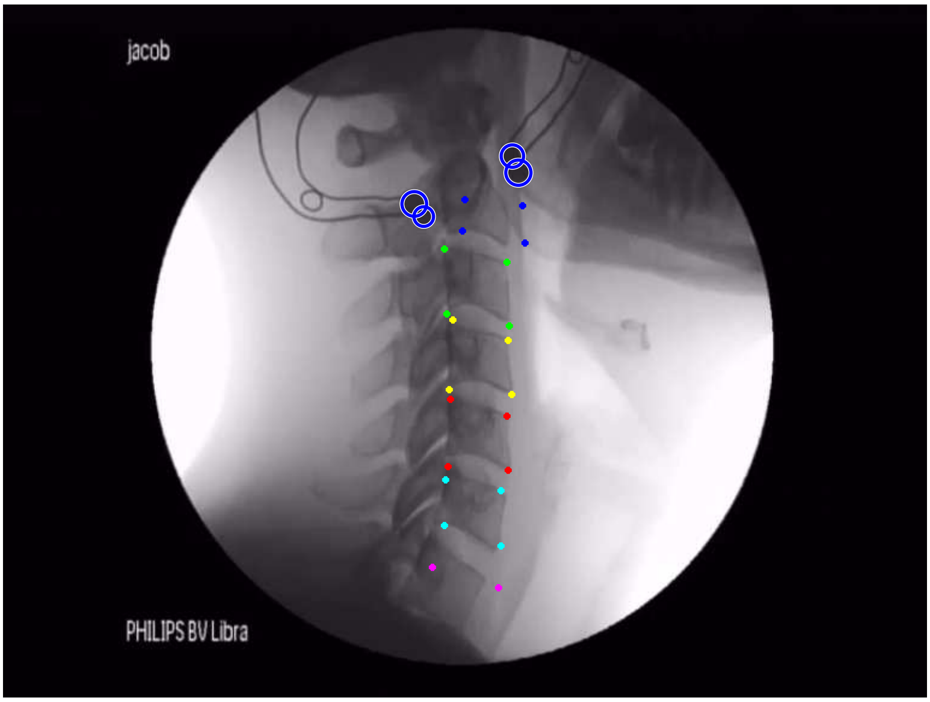

Figure 5.8: The result of the automatic detection method for *Fluoroscopic recording 6* with the vertebral corner points of C2-C7 and delineated external markers.

Fluoroscopic recording 7

The result of the seventh fluoroscopic recording is represented by a frame shown in *Figure 5.9*. All four external markers have been correctly detected in all tested frames.

The corners of C3-C6 have been detected somewhat close to the true corners, while the same only applies for the dorsal corner point of C7. Both inferior corner points of C2 and the ventral point of C7 are far from the true locations.

All five of the tested frames resulted in successful detection using the automatic detection method. For *Fluoroscopic recording 7*, the average duration of automatic detection in the five frames was 3 minutes and 57 seconds.

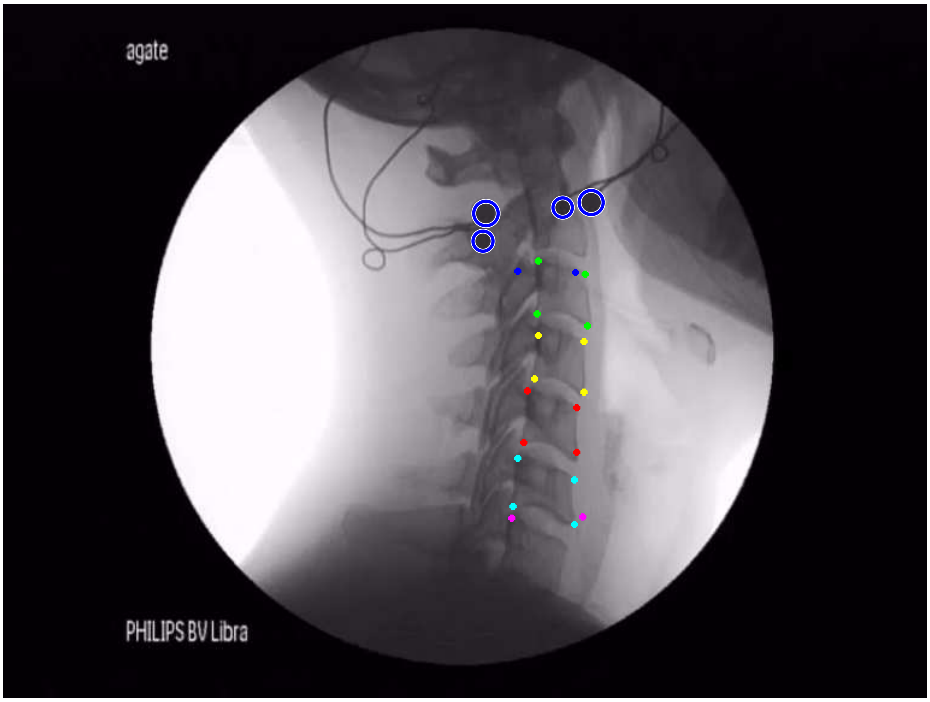

Figure 5.9: The result of the automatic detection method for *Fluoroscopic recording 7* with the vertebral corner points of C2-C7 and delineated external markers.

Fluoroscopic recording 8

A result of the eighth fluoroscopic recording is shown in *Figure 5.10*, where all four external markers have been correctly detected although the two most ventral external markers overlap in the image. The external markers were detected correctly in all five tested frames.

The method for detecting the inferior corner points of C2 has resulted in a satisfying detection of the ventral corner point while the dorsal point is located posterior to the vertebral body of C3. The superior ventral corner point of C3 is inaccurate, but apart from that, the ventral corner points are in general quite well detected. The same applies for the two superior corner points of C7.

As in *Fluoroscopic recording 3* and *Fluoroscopic recording 7*, the automatic detection method was able to detect C2-C7 in all five of the tested frames. Furthermore, the tested frames had the shortest average duration of 3 minutes and 26 seconds.

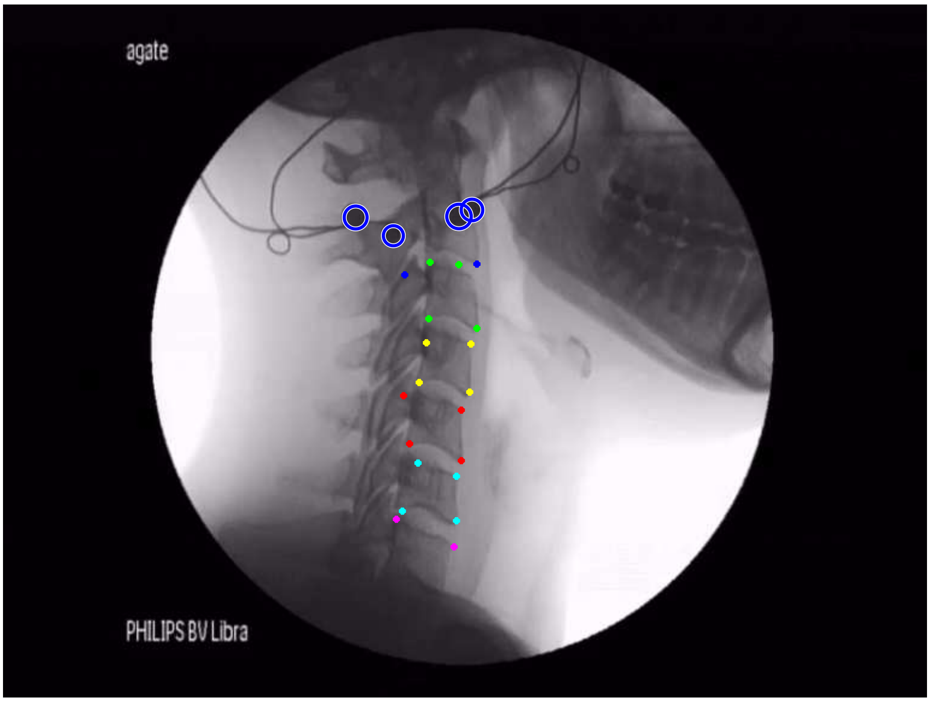

Figure 5.10: The result of the automatic detection method for *Fluoroscopic recording 8* with the vertebral corner points of C2-C7 and delineated external markers.

Chapter 6

Discussion

The aim of this thesis was to develop a fully automatic method for corner point detection of the cervical vertebrae in fluoroscopic images. Several semi-automatic methods have been described, however, they all involved a manual definition of the vertebral body. Most of the automatic detection methods were conducted in the less noisy images using radiography, and the majority of the methods utilized machine learning, which required a large data set. No previous methods automatically detecting the cervical vertebrae in fluoroscopic images have been found. The idea was to develop a detection method without the requirements of a large data set, but suitable for any fluoroscopic recording of the cervical spine.

The automatic detection method utilizes simple algorithms, and it is the combinations of these that enable the automatic detection of the vertebral landmarks. The different combinations of the algorithms in the multi-segmentation approach attempt to take various cases of poor contrast into account, however, obviously not all. This leads to location of C2 and C7 in several images, where the multi-segmentation approach is unable to detect the true edges of the vertebral bodies. Also C1 is often located, but due to its very different anatomical shape, which has not been considered, the landmarks of this vertebra are not detected.

The initial objective of the specified aim was to automatically locate the cervical vertebral bodies C3-C6 in a fluoroscopic image. This was successful to all the available eight fluoroscopic recordings. The first five frames of each fluoroscopic recording, before the onset of movement, were tested. Of the 40 tested frames, the method was able to detect all four external markers correctly in 27 frames, while C2-C7 were detected in 31 of the 40 frames. C3-C6 were not identified correctly in all of the tested frames, but all were found in a minimum of two of the first five frames. The vertebral bodies of C3-C6 were located using a template with their average anatomical shape, based on visual evaluation, to find similar shapes. For locating C1, C2 and C7, the use of customized templates could be included for the search.

The second objective was to automatically detect the four landmarks in each of the four localized vertebral bodies C3-C6. Due to the fact that a single segmentation was not able to take every case of poor contrast between the vertebral body and the background into account, a multi-segmentation approach was utilized. In a few cases, the four corners of all vertebral bodies C2-C7 were found using this method, but most often the inferior corners of C2 and the superior corners of C7 were found subsequently.

If the vertebral bodies of C2 and C7 were not detected either by the template matching or through the multi-segmentation approach, the inferior corners of C2 and the superior corners of C7 were found, based on the location of C3 and C6, respectively. In this case, only one segmentation was performed for each of the vertebrae C2 and C7, which often resulted in detection of just one of the two corner points or none at all. In order to improve the detection of the vertebral corner points, a multi-segmentation approach, similar to the one used for the detection of the vertebral corners of C3-C6, could be utilized, where the location of C2 and C7 would be based on either different templates or the known locations of C3 and C6.

The visual validation suggests promising results of the automatic detection method, but also clarifies the requirements for further refinements to increase the robustness. The method is generally more precise when locating the ventral corner points compared to the dorsal. This is most likely due to the higher contrast between the ventral vertebral edge and the background, compared to the low contrast between the dorsal edge of the vertebral body and the spinous processes. The visual validation could be supported by a comparison to manual markings, which are often considered to be ground truth.

The duration was measured in all the tested frames with a total average of 4 minutes and 13 seconds. The automatic detection method should be optimized in order to obtain a shorter duration in case of implementation.

Conclusion

It has been proven that it is possible to automatically detect the external markers and the corner points of the vertebral bodies C2-C7, using the developed automatic detection method. The method was tested on the first five frames of the eight fluoroscopic recordings, and C2-C7 were detected in 31 of the 40 tested frames.

The method is promising but requires further development to be able to detect C1 and more precise corner points of C2 and C7. Furthermore, an optimization of the duration should be considered.

References

Horst Aichinger, Joachim Dierker, Sigrid Joite-Barfuß, and Manfred Säbel. *Radiation Exposure and Image Quality in X-Ray Diagnostic Radiology*. Springer Berlin Heidelberg, 2012. doi: 10.1007/978-3-642-11241-6.

S. M. Al-Arif, M. Asad, K. Knapp, M. Gundry, and G.G. Slabaugh. Hough forest-based corner detection for cervical spine radiographs. In *Paper presented at the Medical Image Understanding and Analysis Conference, MIUA 2015*, 2015a. 15-07-2015 - 17-07-2015, University of Lincoln, UK.

S M Masudur Rahman Al-Arif, Muhammad Asad, Karen Knapp, Michael Gundry, and Greg Slabaugh. Cervical vertebral corner detection using haar-like features and modified hough forest. In *2015 International Conference on Image Processing Theory, Tools and Applications (IPTA)*. IEEE, nov 2015b. doi: 10.1109/IPTA.2015.7367179.

S. M. Masudur Rahman Al-Arif, Karen Knapp, and Greg Slabaugh. Fully automatic cervical vertebrae segmentation framework for x-ray images. *Computer Methods and Programs in Biomedicine*, 157:95–111, apr 2018. doi: 10.1016/j.cmpb.2018.01.006.

William J. Anderst, William F. Donaldson, Joon Y. Lee, and James D. Kang. Cervical spine intervertebral kinematics with respect to the head are different during flexion and extension motions. *Journal of Biomechanics*, 46(8):1471–1475, may 2013a. doi: 10.1016/j.jbiomech.2013.03.004.

William J. Anderst, Joon Y. Lee, William F. Donaldson, and James D. Kang. Six-degrees-of-freedom cervical spine range of motion during dynamic flexion-extension after single-level anterior arthrodesis. *The Journal of Bone and Joint Surgery*, 95(6):497–506, mar 2013b. doi: 10.2106/JBJS.K.01733.

William J. Anderst, Tom Gale, Clarissa LeVasseur, Sandesh Raj, Kris Gongaware, and Michael Schneider. Intervertebral kinematics of the cervical spine before, during, and after high-velocity low-amplitude manipulation. *The Spine Journal*, aug 2018. doi: 10.1016/j.spinee.2018.07.026.

Mathieu Aubry, Sylvain Paris, Samuel W. Hasinoff, Jan Kautz, and Frédo Durand. Fast local laplacian filters. *ACM Transactions on Graphics*, 33(5):1–14, sep 2014. doi: 10.1145/2629645.

Michele C. Battié, Stanley J. Bigos, Ann Sheehy, and Mark D. Wortley. Spinal flexibility and individual factors that influence it. *Physical Therapy*, 67(5):653–658, may 1987. doi: 10.1093/ptj/67.5.653.

Mohammed Benjelloun and Saïd Mahmoudi. Spine localization in x-ray images using interest point detection. *Journal of Digital Imaging*, 22(3):309–318, feb 2008. doi: 10.1007/s10278-007-9099-3.

P. Bifulco, M. Cesarelli, R. Allen, M. Sansone, and M. Bracale. Automatic recognition of vertebral landmarks in fluoroscopic sequences for analysis of intervertebral kinematics. *Medical and Biological Engineering and Computing*, 39(1):65–75, Jan 2001. ISSN 1741-0444. doi: 10.1007/BF02345268. URL https://doi.org/10.1007/BF02345268.

P. Bifulco, M. Cesarelli, M. Romano, R. Allen, and T. Cerciello. Vertebrae tracking through fluoroscopic sequence: a novel approach. In *IFMBE Proceedings*, pages 619–622. Springer Berlin Heidelberg, 2009. doi: 10.1007/978-3-642-03882-2_164.

Paolo Bifulco, Mario Cesarelli, Tommaso Cerciello, and Maria Romano. A continuous description of intervertebral motion by means of spline interpolation of kinematic data extracted by videofluoroscopy. *Journal of Biomechanics*, 45(4):634–641, feb 2012. doi: 10.1016/j.jbiomech.2011.12.022.

Paolo Bifulco, Mario Cesarelli, Maria Romano, Antonio Fratini, and Mario Sansone. Measurement of intervertebral cervical motion by means of dynamic x-ray image processing and data interpolation. *International Journal of Biomedical Imaging*, 2013:1–7, 2013. doi: 10.1155/2013/152920.

Alan C. Breen, Deydre S. Teyhen, Fiona E. Mellor, Alexander C. Breen, Kris W. N. Wong, and Adam Deitz. Measurement of intervertebral motion using quantitative fluoroscopy: Report of an international forum and proposal for use in the assessment of degenerative disc disease in the lumbar spine. *Advances in Orthopedics*, 2012:1–10, 2012. doi: 10.1155/2012/802350.

Jerrold T. Bushberg, J. Anthony Seibert, and Edwin M. Leidholdt. *Essential Physics of Medical Imaging*. LIPPINCOTT RAVEN, third edition, 2011. ISBN 978-0-7817-8057-5. URL https://www.ebook.de/de/product/15362124/jerrold_t_bushberg_j_anthony_seibert_edwin_m_leidholdt_essential_physics_of_medical_imaging.html.

T. Cerciello, P. Bifulco, M. Cesarelli, M. Romano, and R. Allen. Automatic vertebra tracking through dynamic fluoroscopic sequence by smooth derivative template matching. In *2009 9th International Conference on Information Technology and Applications in Biomedicine*. IEEE, nov 2009. doi: 10.1109/itab.2009.5394328.

T. Cerciello, M. Romano, P. Bifulco, M. Cesarelli, and R. Allen. Advanced template matching method for estimation of intervertebral kinematics of lumbar spine. *Medical Engineering & Physics*, 33(10):1293–1302, dec 2011. doi: 10.1016/j.medengphy.2011.06.009.

Michael Y. M. Chen, Thomas L. Pope, and David J. Ott. *Basic Radiology*. McGraw-Hill Education Ltd, second edition, 2010. ISBN 0071627081. URL https://www.ebook.de/de/product/11724304/michael_y_m_chen_thomas_l_pope_david_j_ott_basic_radiology.html. Chs. 1,2,13.

Rajat Chowdhury, Iain Wilson, Christopher Rofe, and Graham Lloyd-Jones. *Radiology at a Glance*. Wiley-Blackwell, 2010. ISBN 9781405192200. URL https://www.amazon.com/Radiology-at-Glance-Rajat-Chowdhury/dp/1405192208?SubscriptionId=AKIAIOBINVZYXZQZ2U3A&tag=chimbori05-20&linkCode=xm2&camp=2025&creative=165953&creativeASIN=1405192208.

Lee R. Dice. Measures of the amount of ecologic association between species. *Ecology*, 26 (3):297–302, jul 1945. doi: 10.2307/1932409.

E. M. Flachs, L. Eriksen, M. B. Koch, J. T. Ryd, E. Dibba, L. Skov-Ettrup, and K. Juel. Sygdomsbyrden i danmark - sygdomme. Statens Institut for Folkesundhed, Syddansk Universitet. Sundhedsstyrelsen, 2015. ISBN 978-87-7104-655-7.

W Frobin, P Brinckmann, G Leivseth, M Biggemann, and O Reikerås. Precision measurement of segmental motion from flexion—extension radiographs of the lumbar spine. *Clinical Biomechanics*, 11(8):457–465, dec 1996. doi: 10.1016/s0268-0033(96)00039-3.

W. Frobin, G. Leivseth, M. Biggemann, and P. Brinckmann. Sagittal plane segmental motion of the cervical spine. a new precision measurement protocol and normal motion data of healthy adults. *Clinical Biomechanics*, 17(1):21–31, jan 2002. doi: 10.1016/s0268-0033(01)00105-x.

Caio Vitor Dos Santos Genebra, Nicoly Machado Maciel, Thiago Paulo Frascareli Bento, Sandra Fiorelli Almeida Penteado Simeão, and Alberto De Vitta. Prevalence and factors associated with neck pain: a population-based study. *Brazilian Journal of Physical Therapy*, 21(4):274–280, jul 2017. doi: 10.1016/j.bjpt.2017.05.005.

Damian Hoy, Lyn March, Peter Brooks, Fiona Blyth, Anthony Woolf, Christopher Bain, Gail Williams, Emma Smith, Theo Vos, Jan Barendregt, Chris Murray, Roy Burstein, and Rachelle Buchbinder. The global burden of low back pain: estimates from the global burden of disease 2010 study. *Annals of the Rheumatic Diseases*, 73(6):968–974, mar 2014a. doi: 10.1136/annrheumdis-2013-204428.

Damian Hoy, Lyn March, Anthony Woolf, Fiona Blyth, Peter Brooks, Emma Smith, Theo Vos, Jan Barendregt, Jed Blore, Chris Murray, Roy Burstein, and Rachelle Buchbinder. The global burden of neck pain: estimates from the global burden of disease 2010 study. *Annals of the Rheumatic Diseases*, 73(7):1309–1315, jan 2014b. doi: 10.1136/annrheumdis-2013-204431.

Eric L. Hurwitz, Kristi Randhawa, Hainan Yu, Pierre Côté, and Scott Haldeman. The global spine care initiative: a summary of the global burden of low back and neck pain studies. *European Spine Journal*, feb 2018. doi: 10.1007/s00586-017-5432-9.

A. Kyle Jones. *Diagnostic Radiology Physics*, chapter 8: Fluoroscopic Imaging Systems, pages 183–207. INTL ATOMIC ENERGY AGENCY, 2014. ISBN 978-92-0-131010-1. URL https://www.ebook.de/de/product/20622679/diagnostic_radiology_physics.html.

Per Kjær, Heidi Eirikstoft, and Inge Ris. Klinisk retningslinje for udredning og klassificering af personer med nakkebesvær. *Danske Fysioterapeuter*, 2010.

V. P. Dinesh Kumar and Tessamma Thomas. Automatic estimation of orientation and position of spine in digitized x-rays using mathematical morphology. *Journal of Digital Imaging*, 18(3):234–241, jun 2005. doi: 10.1007/s10278-005-5150-4.

Mohamed Amine Larhmam, Said Mahmoudi, and Mohammed Benjelloun. Semi-automatic detection of cervical vertebrae in x-ray images using generalized hough transform. *International Journal of Computer Assisted Radiology and Surgery*, 9(2):177–187, March 2012. doi: 10.1109/IPTA.2012.6469570.

Mohamed Amine Larhmam, Mohammed Benjelloun, and Saïd Mahmoudi. Vertebra identification using template matching modelmp and k -means clustering. *International Journal of Computer Assisted Radiology and Surgery*, 9(2):177–187, jul 2013. doi: 10.1007/s11548-013-0927-2.

Fabian Lecron, Mohammed Benjelloun, and Saïd Mahmoudi. Fully automatic vertebra detection in x-ray images based on multi-class SVM. In David R. Haynor and Sébastien Ourselin, editors, *Medical Imaging 2012: Image Processing*. SPIE, feb 2012a. doi: 10.1117/12.911424.

Fabian Lecron, Mohammed Benjelloun, and Saïd Mahmoudi. Cervical spine mobility analysis on radiographs: A fully automatic approach. *Computerized Medical Imaging and Graphics*, 36(8):634–642, dec 2012b. doi: 10.1016/j.compmedimag.2012.08.004.

David Lisle. *Imaging for Students*. Taylor & Francis Ltd., fourth edition, 2012. ISBN 978-1-444-121-827. URL https://www.ebook.de/de/product/18146187/david_lisle_imaging_for_students.html. Chs. 1,9.

Frederic H. Martini, Judi L. Nath, and Edwin F. Bartholomew. *Fundamentals of Anatomy & Physiology*. Benjamin Cumings, Paperback(2011), ninth edition, 2012. ISBN 978-0321-73553-9.

Muhammad Nauman, Ali Hassan, Farhan Riaz, Saad Rehman, Rasmus Wiberg Nedergard, Kelly Holt, Heidi Haavik, and Imran Khan Niazi. Automatic tracking of cervical spine using fluoroscopic sequences. In *2017 Intelligent Systems Conference (IntelliSys)*. IEEE, sep 2017. doi: 10.1109/intellisys.2017.8324355.

Anne Krogh Nøhr, Louise Pedersen Pilgaard, Bolette Dybkjær Hansen, Rasmus Nedergaard, Heidi Haavik, Rene Lindstroem, Maciej Plocharski, and Lasse Riis Østergaard. Semi-automatic method for intervertebral kinematics measurement in the cervical spine. In *Image Analysis*, pages 302–313. Springer International Publishing, 2017. doi: 10.1007/978-3-319-59129-2_26.

Simon Just Kjeldgaard Pedersen. Circular hough transform. *Aalborg University, Vision, Graphics, and Interactive Systems*, November 2007.

P. Perona and J. Malik. Scale-space and edge detection using anisotropic diffusion. *IEEE Transactions on Pattern Analysis and Machine Intelligence*, 12(7):629–639, jul 1990. doi: 10.1109/34.56205.

S.M. Pizer, R.E. Johnston, J.P. Ericksen, B.C. Yankaskas, and K.E. Muller. Contrast-limited adaptive histogram equalization: speed and effectiveness. In *[1990] Proceedings of the First Conference on Visualization in Biomedical Computing*. IEEE Comput. Soc. Press, 1990. doi: 10.1109/vbc.1990.109340.

Maciej Plocharski, Rene Lindstroem, Cassandra Frydendal Lindstroem, and Lasse Riis Østergaard. Motion analysis of the cervical spine during extension and flexion: Reliability of the vertebral marking procedure. *Medical Engineering & Physics*, aug 2018. doi: 10.1016/j.medengphy.2018.07.010.

Rianne Reinartz, Bram Platel, Toon Boselie, Henk van Mameren, Henk van Santbrink, and Bart ter Haar Romeny. Cervical vertebrae tracking in video-fluoroscopy using the normalized gradient field. In *Medical Image Computing and Computer-Assisted Intervention – MICCAI 2009*, pages 524–531. Springer Berlin Heidelberg, 2009. doi: 10.1007/978-3-642-04268-3_65.

Deydre S. Teyhen, Timothy W. Flynn, John D. Childs, Timothy R. Kuklo, Michael K. Rosner, David W. Polly, and Lawrence D. Abraham. Fluoroscopic video to identify aberrant lumbar motion. *Spine*, 32(7):E220–E229, apr 2007. doi: 10.1097/01.brs.0000259206.38946.cb.

S P Vimal and P K Thiruvikraman. Automated image enhancement using power law transformations. *Sadhana*, 37(6):739–745, dec 2012. doi: 10.1007/s12046-012-0110-4.

Xu Wang, René Lindstroem, Maciej Plocharski, Lasse Riis Østergaaard, and Thomas Graven-Nielsen. Cervical flexion and extension includes anti-directional cervical joint motion in healthy adults. *The Spine Journal*, 18(1):147–154, jan 2018. doi: 10.1016/j.spinee.2017.07.170.

Xi Xu, Hong-Wei Hao, Xu-Cheng Yin, Ning Liu, and Shawkat Hasan Shafin. Automatic segmentation of cervical vertebrae in x-ray images. In *The 2012 International Joint Conference on Neural Networks (IJCNN)*. IEEE, jun 2012. doi: 10.1109/ijcnn.2012.6252793.

Ping Xue and David L. Wilson. Effects of motion blurring in x-ray fluoroscopy. *Medical Physics*, 25(5):587–599, may 1998. doi: 10.1118/1.598240.

Yalin Zheng, M. S. Nixon, and R. Allen. Automatic lumbar vertebrae segmentation in fluoroscopic images via optimised concurrent hough transform. In *Conference Proceedings of the 23rd Annual International Conference of the IEEE Engineering in Medicine and Biology Society*. IEEE, 2001. doi: 10.1109/IEMBS.2001.1017328.

Kelly H. Zou, Simon K. Warfield, Aditya Bharatha, Clare M.C. Tempany, Michael R. Kaus, Steven J. Haker, William M. Wells, Ferenc A. Jolesz, and Ron Kikinis. Statistical validation of image segmentation quality based on a spatial overlap index1. *Academic Radiology*, 11(2):178–189, feb 2004. doi: 10.1016/S1076-6332(03)00671-8.